A Density-Dependent Reaction-Diffusion Model of Pore Bridging in Tissue-Regenerating Scaffolds under Oxygen Limitation

Annika Nikhar[1,2], Adelaide Cagle[2], Katherine Hixon[2], Peter Mucha[1]

[1]Department of Mathematics, Dartmouth College, 29 N. Main Street, Hanover, 03755, NH, USA.

[2] Thayer School of Engineering, Dartmouth College, 15 Thayer Drive, Hanover, 03755, NH, USA.

Abstract

Uniform cell infiltration is essential for engineering homogeneous and mechanically integrated soft tissue, yet under static culture oxygen reaches a scaffold only by diffusion from its exposed surface. Top-seeded cells settle most densely near that surface, where their oxygen consumption can outpace diffusive resupply and starve deeper regions. Whether this is enough to alter tissue formation has been difficult to test experimentally. We develop a reduced multiscale model that couples scaffold-scale oxygen transport to pore-scale bridging in one direction, justified by a separation of timescales. A quasi-steady reaction-diffusion equation resolves oxygen over a prescribed, exponentially attenuating cell density, while a degenerate Porous-Fisher equation in spherical geometry, with oxygen-modulated proliferation, drives the bridging front. Nondimensionalization reduces the system to a few dimensionless groups and yields a closed-form critical depth separating consumption- from diffusion-dominated regions. The model predicts a trade-off in which higher seeding accelerates bridging near the surface but, by depleting oxygen at depth, narrows the band over which pores bridge at all. This pinpoints the scaffold thicknesses and seeding densities where oxygen limitation yields uneven tissue.

Contents

1 Introduction

1.1 Biological Motivation

Skin and soft tissue are some of the body's primary mechanical and immunological barriers, responsible for retaining moisture, resisting infection, and maintaining structural integrity following injury. While skin possesses intrinsic regenerative capacity, this capacity is often insufficient in the context of large-area wounds, chronic injuries, or sites requiring interface with long-term implanted devices like osseointegrated prosthetics, permanent intravenous access ports, and ostomy stomas [1]. In such settings, the failure to reestablish a continuous, sealed dermal barrier creates pathways for bacterial ingress, hypersensitivity reactions, impaired wound healing, and implant loosening [2]. More broadly, the challenge of engineering uniform and mechanically

integrated soft tissue remains a central unsolved problem in regenerative medicine.

Tissue engineering offers a promising approach to these challenges by providing engineered scaffolds that support cell adhesion, proliferation, and migration while guiding new tissue formation. For successful regeneration, scaffolds must permit deep and spatially uniform cell ingrowth, ensuring complete tissue coverage and mechanical continuity throughout the construct. Heterogeneous cell infiltration, in which cells colonize the scaffold unevenly, produces mechanically weak tissue and compromises long-term implant stability [3]. Understanding and controlling the spatial dynamics of cell infiltration is therefore essential for the rational design of scaffolds intended for tissue repair.

Biomaterial cryogel scaffolds are particularly promising for these applications. These mechanically durable, macroporous constructs comprise an interconnected network with high porosity and large pore sizes, typically around 100 μm [1]. Their resilience and architecture have led to their use across a range of tissue-engineering applications, providing ample space for cell attachment, migration, and proliferation. As cells colonize the scaffold, they adhere to pore walls, migrate inward, and proliferate to progressively fill the pore lumen. This process is referred to as pore bridging or pore infilling. Complete and uniform pore bridging throughout the scaffold is essential for forming continuous and mechanically integrated tissue.

Under static culture conditions, oxygen is supplied to the scaffold exclusively by diffusion from the surrounding culture medium [4]. Cells consume oxygen via oxidative phosphorylation, among other aerobic processes, to sustain their metabolic activity and proliferate. When cell density is sufficiently high, local oxygen consumption can outpace diffusive supply and generate concentration gradients across the scaffold depth. In scaffolds with dimensions exceeding a few millimeters, reduced oxygen availability in deeper regions can hinder cell proliferation and, by extension, the rate and completeness of pore bridging [5].

The cell seeding mode therefore becomes a factor influencing spatial heterogeneity. When cells are loaded from the top surface of a scaffold, they settle and adhere within the first several hours, establishing a depth-dependent distribution where cell density is highest near the seeding surface and attenuates with depth [6]. This non-uniform distribution can drive strong oxygen consumption near the top of the scaffold, where cell density is greatest, potentially producing local depletion that suppresses proliferation. The interplay between cell density dynamics and oxygen limitation, and the seeding and scaffold conditions under which it becomes significant, remains poorly understood.

Despite established experimental results on cryogel scaffolds, quantitative relationships linking cell loading, oxygen transport, and pore bridging dynamics remain underexplored. The biological problem can be stated as follows: under static culture, a depth-dependent seeding profile and limited diffusive oxygen supply are together expected to produce spatially heterogeneous tissue formation, but it is not known

under what conditions of scaffold thickness and cell loading this heterogeneity becomes meaningful. This biological problem admits a corresponding mathematical formulation, which may be framed as reaction–diffusion dynamics across two spatial scales: a quasi-steady reaction–diffusion oxygen field, set by a prescribed depth-dependent cell density at the scaffold scale, coupled in one direction to a degenerate, density-dependent reaction–diffusion (Porous–Fisher) equation governing the inward advance of the cell front at the pore scale. The central mathematical objective is to characterize how the speed of the bridging front, and hence the pore-bridging time, varies with depth as a function of scaffold thickness and cell loading.

Mathematical modeling provides a controlled means of investigating these relationships, particularly given the difficulty of obtaining accurate in vitro measurements of oxygen availability and cell behavior within three-dimensional constructs. By resolving the one-way coupling between scaffold-scale oxygen transport and pore-scale bridging dynamics, the multiscale framework proposed here aims to predict spatially heterogeneous tissue growth within macroporous scaffolds. It offers a quantitative basis for understanding how scaffold thickness, seeding density, and pore geometry might be engineered to achieve uniform tissue formation in future scaffold design.

1.2 Research Goals

This thesis develops a multiscale model of cell-mediated pore infilling in three-dimensional macroporous cryogel scaffolds under static culture, in order to determine if and how oxygen limitation can affect spatial heterogeneity in tissue formation. At the pore scale (microscale), tissue forms as individual pores are bridged by cells: within a representative pore of radius R, cell density evolves through density-dependent migration and oxygen-modulated logistic proliferation [7]. At the scaffold scale (macroscale), the initial adhesion of cells to scaffold struts establishes a depth-dependent cell density across the vertical coordinate z, over which oxygen availability varies through diffusion from the surrounding medium and consumption by the metabolically active cells present.

The seeding process is described in three main stages. First, cells in suspension are transported into the pore network by gravity and convective flow [3]. Second, cells contact scaffold surfaces and adhere via interactions of charge and protein domains[6]. The resulting depth-dependent distribution is established, highest near the seeding surface and attenuating with depth. Individual pores, although irregular in shape, are treated as approximately spherical with characteristic radius R. Cells initially occupy a thin annular region near the pore wall and subsequently migrate inward and proliferate, progressively filling the pore lumen.

The model is intentionally reduced. Rather than solving a fully coupled system, in which scaffold-scale cell density, oxygen dynamics, and pore-scale evolution affect each other with bidirectional feedback, it isolates the specific mechanism of interest: whether realistic scaffold-scale seeding densities can produce oxygen depletion strong enough to alter pore-scale bridging. To this end, a one-way coupled architecture is adopted,

in which the fields are resolved sequentially:

$$\rho_{\text{eff}} \rightarrow c(z) \rightarrow u(r, t; z_i).$$

ρ_{eff} is the prescribed scaffold-scale cell density, $c(z)$ the resulting quasi-steady oxygen profile, and $u(r, t; z_i)$ is the cell density within a pore at depth z_i. The scaffold-scale oxygen field sets the local proliferation rate within each pore, while pore-scale dynamics are assumed not to alter the scaffold-scale cell distribution over the timescale of interest. This reduction avoids the introduction of poorly constrained parameters associated with cell redistribution and keeps the model computationally tractable. The primary model output is the finite-time pore closure rate, v_{eff}, quantifying how fast tissue may grow within a pore and serving as a proxy for hypoxic effects.

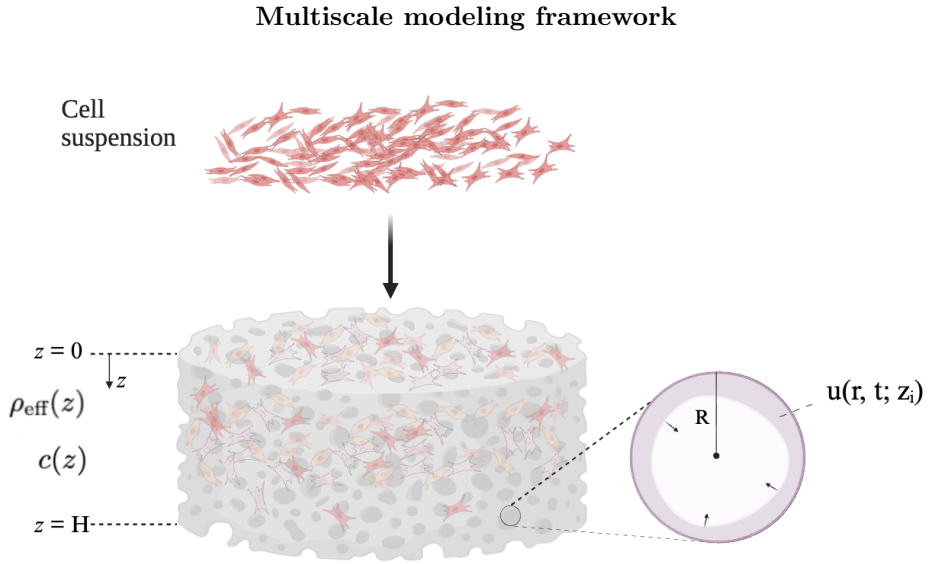

Fig. 1: Cells seeded at the top surface ($z = 0$) create a depth-dependent distribution. Oxygen transport is modeled along the coordinate z, while pore-scale dynamics at depth z_i are represented radially, such that $u(r, t; z_i)$ evolves inward via migration and proliferation to drive pore bridging.

The central question motivating the model is: under what conditions of scaffold thickness and cell loading does oxygen depletion become sufficient to measurably alter pore-scale bridging dynamics? By way of the model, nondimensional analysis, and numerical simulation, the thesis addresses three specific research questions:

1. Where and under what conditions does oxygen depletion occur, and can the consumption-to-diffusion transition be characterized across scaffold depth?

2. How does degenerate, density-dependent diffusion in spherical geometry govern the shape and speed of the pore-bridging front, relative to the planar traveling-wave speed of the corresponding linear Fisher–KPP model?
3. When scaffold-scale oxygen dynamics are coupled to pore-scale proliferation, does the resulting front velocity exhibit emergent depth-dependent heterogeneity, and in which parameter regimes is this effect significant rather than negligible?

2 Mathematical Model

2.1 Modeling Assumptions

The model rests on several simplifying assumptions. The scaffold is submerged and cultured in static media, and is bounded on all sides except for its top surface by well-plate walls. Therefore, oxygen can only be supplied only through the exposed top surface, and it moves down the scaffold's vertical axis by passive diffusion under static culture, with no convective transport [8]. Oxygen also diffuses far faster than cells migrate or proliferate, so its profile is treated as quasi-steady, adjusting instantaneously to the surrounding cell density rather than evolving in time. Within a single pore, which is about eight orders of magnitude smaller than a scaffold, oxygen is treated as uniform such that all cells in a pore at depth z_i experience the same concentration $c(z_i)$.

Cell density over the scaffold's depth, $\rho_{\text{eff}}(z)$, is a prescribed input rather than a quantity that the model evolves. In particular, the oxygen solution $c(z)$ is computed only once and is not recomputed as cells proliferate and fill the pore; the model does not track additional oxygen that the growing cells would consume.

At the model's microscale, each pore is idealized as a sphere of radius R, and cell growth is assumed radially symmetric such that cell density u only depends on the distance from the pore center. Cells are described as a continuum, spreading by density-dependent diffusion that slows in sparsely populated regions and produces a sharp advancing front [5]. Oxygen influences only the proliferation rate and is assumed not to affect cell motility.

The pore-scale clock starts once seeding is complete: the depth-dependent profile forms within hours as cells settle and adhere, so the seeding interval is treated as preceding $t = 0$, with all migration and proliferation occurring afterward. At $t = 0$, the adherent cells form a thin layer against the pore wall, later described by a Gaussian initial condition. The Gaussian serves only as an initial wall-localized cell distribution, after which the Porous-Fisher equation governs all later evolution. The pore is then treated as closed, with no cells entering or leaving through the wall, so bridging proceeds entirely by inward migration and proliferation of the initially adherent cells. Finally, scaffold properties including porosity, pore size, and material parameters are assumed uniform and unchanging over the experimental timescale, with degradation and remodeling neglected .

2.2 Mathematical Formulation

2.2.1 Macroscopic Modeling: Scaffold-Scale Cell Density Dynamics

At the scaffold-scale, cells are introduced as a suspension onto the top surface, where they penetrate the pore network under gravity and are progressively captured by scaffold struts through adhesion. As the suspension descends, cells are captured at a rate proportional to local concentration. The scaffold-scale effective cell density $\rho_{\text{eff}}(z)$ describes the spatial distribution of this adherent population after seeding is complete. Its initial condition is taken at the scaffold's top surface, $z = 0$, such that $\rho_{\text{eff}}(0) = \rho_0$. Thus, the governing equation for the depth-dependent change in ρ_{eff} is given by

$$\frac{d\rho_{\text{eff}}}{dz} = -\beta\rho_{\text{eff}}(z),\ \rho_{\text{eff}}(0) = \rho_0, \tag{1}$$

where $\beta > 0$ is the attenuation coefficient reflecting the rate of cell capture per unit depth. Given the large pore network and surface area of cryogel scaffolds, β is expected to be large relative to scaffold height H, producing steep exponential attenuation of cell density with depth. The solution to equation (1) gives,

$$\rho_{\text{eff}}(z) = \rho_0 e^{-\beta z}, \tag{2}$$

and the spatial shape of this profile is assumed fixed over the timescale of pore bridging, consistent with the biological observation that the seeding-determined depth profile is established well before active bridging.

ρ_0 can be determined from the total adherent cell number, N_{adhered}.

$$N_{\text{adhered}} = \int_0^H \rho_{\text{eff}} A dz = \int_0^H \rho_0 e^{-\beta z} A dz = A\rho_0 \frac{1 - e^{-\beta H}}{\beta} \tag{3}$$

Where A is the bulk scaffold cross-sectional area. Therefore,

$$\rho_0 = \frac{N_{\text{adhered}}\beta}{A(1 - e^{-\beta H})}, \tag{4}$$

assuming that all seeded cells ultimately adhere to pore walls, which may be interpreted as an upper bound on ρ_0 for a given total seeded cell number.

2.3 Macroscopic Modeling: Scaffold-Scale Oxygen Dynamics

Let $c(z, t)$ denote the oxygen concentration at depth $z \in [0, H]$. The mass balance of oxygen within the scaffold is governed by Fick's law with a reaction term[8],

$$\frac{\partial c(z,t)}{\partial t} = D_c \frac{\partial^2 c(z,t)}{\partial z^2} - F(c, \rho_{\text{eff}}(z)),\ 0 < z < H. \tag{5}$$

Here, D_c is the effective oxygen diffusivity within the scaffold. Cellular oxygen consumption, F, is modeled using Michaelis-Menten kinetics yielding

$$F(c, \rho_{\text{eff}}(z)) = \frac{V_{\max}\rho_{\text{eff}}(z)c}{K_m + c}, \tag{6}$$

where $V_{\max}$ is the maximum oxygen consumption rate per cell and K_m is the Michaelis half-saturation constant. The governing equation becomes,

$$\frac{\partial c}{\partial t} = D_c\frac{\partial^2 c}{\partial z^2} - \frac{V_{\max}\rho_{\text{eff}}(z)c}{K_m + c}. \tag{7}$$

Under the quasi-steady assumption, the time derivative $\partial c/\partial t$ vanishes. The scaffold-scale oxygen equation therefore only depends on depth z, and the equation reduces to

$$0 = D_c\frac{\partial^2 c}{\partial z^2} - \frac{V_{\max}\rho_{\text{eff}}(z)c}{K_m + c}. \tag{8}$$

Oxygen concentration $c(z)$ is assumed spatially uniform within individual pores, since pore radii are much smaller than scaffold height. For a pore specified at depth z_i, the local oxygen concentration is given by $c(z_i)$.

Because oxygen enters exclusively through the top surface at $z = 0$, a Dirichlet boundry condition is imposed,

$$c(0) = c_{\text{media}}. \tag{9}$$

The bottom face is impermeable to oxygen exchange, giving a no-flux condition

$$\frac{\partial c}{\partial z}(H) = 0. \tag{10}$$

These two conditions fully determine the nonlinear boundary value problem for $c(z)$. The quasi-steady oxygen profile $c(z)$ is taken to represent the equilibrated state following seeding, consistent with the rapid timescale of oxygen diffusion across millimeter distances relative to the timescale of cell migration and proliferation. No initial condition is required for $c(z)$ because the quasi-steady assumption eliminates the time derivative; at the timescale of cell dynamics, the oxygen profile adjusts instantaneously to any change in $\rho_{\text{eff}}(z)$.

2.4 Microscopic Modeling: Pore-Scale Cell Density Dynamics

2.4.1 Inspiration

The microscale model is inspired by reaction-diffusion equations used to study biological invasion. The standard Fisher-KPP equation,

$$\frac{\partial u}{\partial t} = D\Delta u + \lambda u\left(1 - \frac{u}{K}\right), \tag{11}$$

combines linear diffusion with logistic growth [9], where D is a constant diffusivity, λ is the intrinsic proliferation rate, and K the carrying capacity. In one spatial dimension, this equation admits traveling waves with solution

$$u(x,t) = f(x - vt), \tag{12}$$

such that the shape of u does not change as f translates at constant speed v. These wave-fronts exist for every speed $v \geq v_{\min} = 2\sqrt{D\lambda}$, and front-like initial data select from the minimum speed $v_{\min} = 2\sqrt{D\lambda}$ [10].

Because diffusivity of the Fisher-KPP equation is constant, it remains active even where u is arbitrarily small. This linear diffusion has an infinite speed of propagation, so any localized initial population becomes positive everywhere instantaneously. The traveling fronts that emerge are correspondingly smooth, with density ahead of the front decaying exponentially rather than terminating at a definite edge. Biologically, this would predict a haze of isolated cells far ahead of the advancing tissue, which is not observed in pore bridging where tissue advances with a recognizable boundary [5].

To obtain a definite tissue edge, the present model instead uses a Porous-Fisher equation, in which diffusivity depends on local cell density,

$$\frac{\partial u}{\partial t} = D_u \nabla \cdot \left(\frac{u}{K} \nabla u \right) + \lambda u \left(1 - \frac{u}{K} \right). \tag{13}$$

The effective diffusivity $D_{\text{eff}} = D_u(u/K)$ vanishes as u approaches 0, such that the equation is degenerate at the advancing tissue front. This degeneracy provides the model with a finite speed of propagation; a region of zero density is not immediately populated by diffusive tails, but is invaded by a front advancing at a finite speed. The equation admits traveling waves for $v \geq v^*$, where the minimum speed

$$v^* = \sqrt{\frac{D_u \lambda}{2}} \tag{14}$$

corresponds to the sharp, compactly supported wave, i.e., the density meets zero at a finite location with discontinuous slope and produces a definite edge. Speeds of $v > v^*$ instead provide smooth fronts with positive tails [10] [11]. This sharp, compactly supported front is the qualitative feature observed by pore bridging, making the Porous-Fisher model optimal.

To incorporate nutrient limitation governed by oxygen availability, the proliferation rate is modified with a Monod factor evaluated at the scaffold depth z_i,

$$\lambda(c(z_i)) = \lambda_{\max} \frac{c(z_i)}{K_s + c(z_i)}, \tag{15}$$

where $\lambda_{\max}$ is the maximum proliferation rate, and K_s is the oxygen half-saturation constant. This function captures the transition from oxygen-limited growth ($c(z_i) \ll$

K_s) to saturated growth ($c(z_i) \gg K_s$) [12]. Substitution yields the Cartesian pore-scale model

$$\frac{\partial u}{\partial t} = D_u \nabla \cdot \left(\frac{u}{K} \nabla u \right) + \lambda_{\max} \frac{c(z_i)}{K_s + c(z_i)} u \left(1 - \frac{u}{K} \right), \tag{16}$$

which combines the degenerate diffusion with logistic proliferation limited by oxygen uptake kinetics.

2.4.2 Spherical Radial Conversion

To better reflect pore geometry of cryogels, the pore-scale model is reformulated in spherical coordinates. While irregular in shape, individual pores are idealized as spherical with characteristic radius R, and under culture conditions, cell adhesion and inward migration are taken to be radially isotropic.

$$u = u(r, \theta, \phi, t; z_i);\ 0 \le r \le R;\ 0 \le \theta \le \pi;\ 0 \le \phi < 2\pi, \tag{17}$$

where r is the radial distance from the pore center, θ is the polar angle, and ϕ is the azimuthal angle.

Cell movement within the pore is described by the flux,

$$\mathbf{J} = -D_u \frac{u}{K} \nabla u. \tag{18}$$

The spherical gradient of the scalar field is

$$\nabla u = \frac{\partial u}{\partial r} \mathbf{e}_r + \frac{1}{r} \frac{\partial u}{\partial \theta} \mathbf{e}_\theta + \frac{1}{r \sin\theta} \frac{\partial u}{\partial \phi} \mathbf{e}_\phi, \tag{19}$$

and divergence of the flux provides the full nonlinear operator

$$\nabla \cdot \left(\frac{u}{K} \nabla u \right) = \frac{1}{r^2} \frac{\partial}{\partial r} \left(r^2 \frac{u}{K} \frac{\partial u}{\partial r} \right) + \frac{1}{r^2 \sin\theta} \frac{\partial}{\partial \theta} \left(\sin\theta \frac{u}{K} \frac{\partial u}{\partial \theta} \right) + \frac{1}{r^2 \sin^2\theta} \frac{\partial}{\partial \phi} \left(\frac{u}{K} \frac{\partial u}{\partial \phi} \right). \tag{20}$$

Under isotropic cell migration and the radially symmetric initial condition discussed in Section 2.4.3, u has no angular dependence so

$$\frac{\partial u}{\partial \theta} = 0 \text{ and } \frac{\partial u}{\partial \phi} = 0. \tag{21}$$

Thus, $u = u(r, t; z_i)$. The angular terms vanish, giving

$$\nabla \cdot \left(\frac{u}{K} \nabla u \right) = \frac{1}{r^2} \frac{\partial}{\partial r} \left(r^2 \frac{u}{K} \frac{\partial u}{\partial r} \right), \tag{22}$$

Expanding the radial diffusion operator using the product rule separates the spherical operator into a planar degenerate-diffusion term and a curvature contribution:

$$\frac{1}{r^2}\frac{\partial}{\partial r}\left(r^2\frac{u}{K}\frac{\partial u}{\partial r}\right) = \left(\frac{u}{K}\frac{\partial u}{\partial r}\right)_r + \frac{2}{r}\frac{u}{K}\frac{\partial u}{\partial r}. \tag{23}$$

The first term is the one-dimensional Cartesian degenerate-diffusion operator. The second term arises from spherical geometry and accounts for the radial flux passing through spherical shells whose surface area scales as $4\pi r^2$. The curvature term serves as a geometric correction required when cell migration is modeled in a spherical pore.

This distinction is important when interpreting front propagation. Classical traveling-wave speeds for Porous-Fisher-type equations are derived in planar domains, where the governing equation is invariant under spatial translation. In the radial pore problem, however, the operator contains the explicit position-dependent factor $2/r$. Therefore, a single constant planar traveling-wave speed does not describe the entire radial closure process. Instead, the planar speed provides a local reference better used away from the pore center, where curvature effects vary more slowly.

Applying the radial operator, stripped of angular dependencies, the spherical Porous-Fisher model reduces to the one-dimensional radial equation

$$\frac{\partial u}{\partial t} = D_u\frac{1}{r^2}\frac{\partial}{\partial r}\left(r^2\frac{u}{K}\frac{\partial u}{\partial r}\right) + \lambda_{\max}\frac{c(z_i)}{K_s + c(z_i)}u\left(1-\frac{u}{K}\right),\ 0 < r < R, \tag{24}$$

producing inward cell migration from the pore wall toward the center. The reaction term is unchanged by the coordinate transformation, as it represents a local process independent of spatial geometry.

2.4.3 Gaussian Initial Conditions

The pore-scale equation for evolving cell density $u(r, t, z_i)$ is solved within a representative spherical pore at scaffold depths z_i, with $r \in [0, R]$ and $u \in [0, K]$. Following the seeding process, cells are assumed to adhere to the scaffold walls and occupy a thin annular region near $r = R$ before any inward migration or proliferation occurs. The initial condition therefore localizes cell density at the pore wall, and is modeled as a Gaussian centered there:

$$u(r, 0; z_i) = a(z_i)\exp\left(-\frac{(R-r)^2}{\sigma^2}\right). \tag{25}$$

$\sigma > 0$ controls the width of the initially occupied rim and the amplitude $a(z_i)$ reflects the local volumetric cell density within the rim at depth z_i, as set by the scaffold-scale cell density distribution ρ_{eff}. Smaller σ produces a sharper, more tightly wall-localized distribution, whereas larger σ produces a broader initial distribution of cells that extends further into the pore interior.

A Gaussian distribution was adopted to describe the rim, preferred over a discontinuous step initial condition, for several reasons. Biologically, initial cell adhesion is not perfect and it is likely that some cells enter the pore interior. Mathematically, a discontinuous step would produce an undefined gradient at its discontinuity. This limitation would also be problematic for the flux-based finite volume method later employed for numerical simulations. The Gaussian instead permits a smooth cell distribution while maintaining strong wall-localization at $t = 0$, such that the flux is well-defined everywhere from the very first time step.

The amplitude $a(z_i)$ is estimated from the seeding conditions. The number of cells adhered to a single pore at depth z_i is given by

$$N(z_i) = \rho_{\text{eff}} \left(\frac{1}{n_{\text{pore}}} \right), \tag{26}$$

where n_{pore} is the pore number density. Distributing these cells over the thin annular shell of volume $4\pi R^2 \sigma$ gives

$$a(z_i) = \min \left(K, \frac{N(z_i)}{4\pi R^2 \sigma} \right), \tag{27}$$

where the operator $\min(K, \cdot)$ ensures that the geometric packing limit of cells cannot be exceeded. The thin shell expression is an approximation: the Gaussian profile is not exactly mass-normalized to $N(z_i)$, but is appropriate for a thin initial layer and avoids the discontinuous annular step. Because cells are typically an order of magnitude smaller than the pore diameter, the thin-rim condition $\sigma \ll R$ holds, and because cell number is not conserved with proliferation, we do not require exact normalization of the initial mass.

Because the Gaussian is strictly positive throughout $[0, R]$, it does not vanish anywhere. The solution therefore possesses no region of exactly zero density and no literal free boundary, which is why the tissue front must be defined operationally as we will see in Section 2.5. It is also worth clarifying that the Gaussian specifies the cell distribution only at $t = 0$, representing the population that has adhered to the pore walls prior to the onset of active bridging. For all $t > 0$, the dynamics are governed entirely by the Porous-Fisher equation, with the inward-directed gradient of the initial distribution serving as the seed from which the bridging front develops.

2.4.4 Boundary Conditions

The representative pore is bounded by its center, $r = 0$ and its wall, $r = R$. At the pore center, the boundary condition must impose regularity and symmetry; a smooth field depending only on the radius, $u = u(r)$, has gradient

$$\nabla u = \frac{\partial u}{\partial r} \mathbf{e}_r.$$

At the origin, the radial direction $\mathbf{e}_r$ is undefined, so the gradient is only continuous if

$$\frac{\partial u}{\partial r}(0, t; z_i) = 0. \tag{28}$$

If this derivative were nonzero, the field would form a conical cusp or carry a directional bias at $r = 0$. This regularity condition is what allows the one-dimensional radial solution to represent a smooth three-dimensional field.

At the pore wall, a representative pore is treated as closed after initialization, so no new cells enter or leave through and all subsequent dynamics arise from the inward migration and proliferation of the initially adherent population. This requires the no-flux condition,

$$\mathbf{J}_r(R, t; z_i) = 0. \tag{29}$$

In the model, both boundary conditions at the pore center and pore wall reduce to the same constraint. While the no-flux condition $\mathbf{J}_r = 0$ is generally weaker than the homogeneous Neumann condition $\partial u/\partial r = 0$, the two differ only where $u = 0$. Because the initial condition is strictly positive and the pore bridging dynamics preserve positivity, $u > 0$ at both boundaries for all t; the factor u/K must be nonzero at both boundary conditions, and $\mathbf{J}_r = 0$ becomes equivalent to $\partial u/\partial r = 0$. Both conditions are therefore written as the homogeneous Neumann condition,

$$\frac{\partial u}{\partial r}(0, t; z_i) = 0 \text{ and } \frac{\partial u}{\partial r}(R, t; z_i) = 0. \tag{30}$$

Additionally, these boundary conditions are consistent with the Gaussian initial condition (25). Differentiating the Gaussian,

$$\frac{\partial u}{\partial r}(r, 0, ; z_i) = a(z_i) \left(\frac{2(R - r)}{\sigma^2} \right) \exp\left(-\frac{(R - r)^2}{\sigma^2} \right). \tag{31}$$

At the wall, $r = R$ and this vanishes exactly since the Gaussian attains its maximum at $r = R$. The initial profile exactly satisfies the wall condition. At the center,

$$\frac{\partial u}{\partial r}(0, 0, ; z_i) = a(z_i) \left(\frac{2R}{\sigma^2} \right) \exp\left(-\frac{R^2}{\sigma^2} \right), \tag{32}$$

which is exponentially small for $\sigma \ll R$, so the initial condition satisfies the regularity condition at $r = 0$ with negligible error. The initial and boundary conditions therefore impose no conflicting constraint at $t = 0$.

2.5 Pore Bridging Analysis

The pore-closure analysis tracks the inward advance of the cell front. While the Porous-Fisher critical speed $v^* = \sqrt{D_u \lambda / 2}$ is the natural reference, certain features of the pore problem cause it to depart from this idealization.

First, the wall-localized Gaussian initial condition (25) satisfies $u(r,0) > 0$ throughout the pore, so the cell density is never zero and the solution has no literal free boundary. The sharp, compactly supported front of the idealized model requires a region of exactly zero density, which the seeded pore does not provide. Although degeneracy still produces a steep front, the front must be defined operationally by crossing of a threshold density. Second, the geometry demanded by the Porous-Fisher model is spherical, rather than planar. The radial operator carries a curvature term whose coefficient $2/r$ grows as the front converges on the center. Therefore, the front speed is not constant but instead accelerates inward; v^* may only hold as a valid reference in a large pore, where curvature is locally weak.

These departures motivate a threshold-based, finite-time description of pore bridging. We introduce a threshold cell density u_c and define the tissue front as the first radial location, moving outward from the center, at which the density reaches it:

$$r_c(t; z_i) = \min\{r \in [0, R] : u(r, t; z_i) \geq u_c\}. \tag{33}$$

As cells invade from the wall, r_c decreases from near R toward 0.

The remaining open pore volume is

$$\Omega(t; z_i) = \frac{4}{3}\pi r_c^3, \tag{34}$$

and when normalized is,

$$\frac{\Omega(t; z_i)}{\Omega(0; z_i)} = \left(\frac{r_c(t; z_i)}{r_c(0; z_i)}\right)^3. \tag{35}$$

At a final culture time t_f, the fractional pore filling can be determined by

$$F_{t_f}(z_i) = 1 - \frac{\Omega(t; z_i)}{\Omega(0; z_i)}, \tag{36}$$

measuring the fraction of the original pore volume deemed occupied based on the desired threshold density.

Because the front speed is non-constant and complete bridging may not occur within a given static culture period, the bridging rate is summarized by an effective finite-time front velocity rather than an instantaneous speed. Over the time interval $[t_1, t_2]$,

$$v_{\text{eff}}(t_1, t_2; z_i) = \frac{r_c(t_1; z_i) - r_c(t_2; z_i)}{t_2 - t_1}, \tag{37}$$

gives the mean inward speed of the threshold front. Computing v_{eff} across scaffold depths can serve as a proxy for predicting heterogeneous tissue formation, and when compared to the depth-dependent $v^*(z_i)$, gives a reference against which the contributions of oxygen limitation, spherical geometry, and finite-domain effects can be gauged.

2.6 Nondimensionalization

We nondimensionalize the scaffold-scale effective cell density using the following scales:

$$\begin{cases} \hat{z} = H^{-1} z \\ \hat{\beta} = \beta H \\ \hat{\rho} = \rho_0^{-1} \rho_{\text{eff}} \end{cases} \tag{38}$$

The change in scaffold-scale cell density then becomes

$$\frac{d\hat{\rho}}{d\hat{z}} = -\hat{\beta}\hat{\rho}, \tag{39}$$

with solution

$$\hat{\rho}(\hat{z}) = e^{-\hat{\beta}\hat{z}} \tag{40}$$

and

$$\hat{\rho}(0) = 1. \tag{41}$$

We nondimensionalize the scaffold-scale oxygen equation using the following scales:

$$\begin{cases} \hat{z} = H^{-1} z \\ \hat{c} = c_{\text{media}}^{-1} c \\ \hat{\rho} = \rho_0^{-1} \rho_{\text{eff}} \end{cases} \tag{42}$$

so that $\hat{c} = 1$ at the top surface.

The oxygen equation becomes

$$0 = \frac{\partial^2 \hat{c}}{\partial \hat{z}^2} - \phi^2 \hat{\rho}(\hat{z}) \cdot \frac{\hat{c}}{1 + \gamma_m \hat{c}}, \tag{43}$$

where

$$\phi^2 = \frac{V_{\max} \rho_0 H^2}{K_m D_c} \text{ and } \gamma_m = \frac{c_{\text{media}}}{K_m}. \tag{44}$$

The dimensionless group ϕ^2 is commonly known as the Thiele modulus and is evaluated at the top-surface density, ρ_0 [3]. γ_m is the oxygen-to-consumption saturation ratio. A more complete proxy of consumption-to-diffusion strength is obtained by preserving depth-dependency, yielding a local Thiele modulus defined as

$$\phi^2_{\text{local}}(\hat{z}) = \phi^2 \hat{\rho}(\hat{z}) = \phi^2 e^{-\hat{\beta}\hat{z}}. \tag{45}$$

The dimensionless Dirichlet boundary condition at the scaffold's top surface is

$$\hat{c}(0) = 1, \tag{46}$$

and the no-flux condition at the scaffold's bottom surface becomes

$$\frac{\partial \hat{c}}{\partial \hat{z}}(1) = 0. \tag{47}$$

We nondimensionalize the microscale cell density model using the following scales:

$$\begin{cases} \hat{r} = R^{-1} r \\ \hat{t} = \lambda_{\max} t \\ \hat{u} = K^{-1} u \\ \hat{c} = c_{\text{media}}^{-1} c \\ \hat{z}_i = H^{-1} z_i \\ \hat{\sigma} = R^{-1} \sigma \end{cases} \tag{48}$$

Thus, the Porous-Fisher equation is given by

$$\frac{\partial \hat{u}}{\partial \hat{t}} = \alpha^2 \frac{1}{\hat{r}^2} \frac{\partial}{\partial \hat{r}} \left(\hat{r}^2 \hat{u} \frac{\partial \hat{u}}{\partial \hat{r}} \right) + \frac{\gamma_s \hat{c}(\hat{z}_i)}{1 + \gamma_s \hat{c}(\hat{z}_i)} \hat{u}(1 - \hat{u}), \ 0 \leq \hat{r} \leq 1. \tag{49}$$

where $\hat{r} = 0$ and $\hat{r} = 1$ represent the pore center and pore wall, respectively, and

$$\hat{\mathbf{J}}_r = -\alpha^2 \hat{u} \frac{\partial \hat{u}}{\partial \hat{r}}, \tag{50}$$

is the radial cell flux. Allowing

$$g(\hat{z}_i) = \frac{\gamma_s \hat{c}(\hat{z}_i)}{1 + \gamma_s \hat{c}(\hat{z}_i)}, \tag{51}$$

to serve as the dimensionless oxygen-modulated parameter, the model may be written more compactly as

$$\frac{\partial \hat{u}}{\partial \hat{t}} = \alpha^2 \frac{1}{\hat{r}^2} \frac{\partial}{\partial \hat{r}} \left(\hat{r}^2 \hat{u} \frac{\partial \hat{u}}{\partial \hat{r}} \right) + g(\hat{z}_i) \hat{u}(1 - \hat{u}), \ 0 \leq \hat{r} \leq 1, \tag{52}$$

with the dimensionless parameters

$$\alpha^2 = \frac{D_u}{R^2 \lambda_{\max}} \text{ and } \gamma_s = \frac{c_{\text{media}}}{K_s}. \tag{53}$$

α^2 serves as a motility-proliferation ratio, and γ_s a oxygen-to-proliferation indicator.

The Gaussian initial condition becomes

$$\hat{u}(\hat{r}, 0; \hat{z}_i) = \tau(\hat{z}_i) \exp\left(\frac{-(1 - \hat{r})^2}{\hat{\sigma}^2} \right), \tag{54}$$

where

$$\tau(\hat{z}_i) = \frac{a(z_i)}{K} \tag{55}$$

is the dimensionless amplitude. For simulation convenience, $\tau(\hat{z}_i)$ is expressed as a depth-dependent function to mitigate the need for dimensional inputs specifying scaffold porosity. We define the Gaussian amplitude τ_0 of a pore located at the scaffold top-surface:

$$\tau_0 = \tau(0) = \min\left(1, \frac{\rho_0 V_{\text{unit}}}{4\pi R^2 \sigma K}.\right). \tag{56}$$

Thus, if no capping occurs, $\tau(\hat{z}_i)$ is reduced to

$$\tau(\hat{z}_i) = \tau_0 e^{-\hat{\beta}\hat{z}_i}. \tag{57}$$

The boundary conditions required by regularity at the radial center and no-flux at the pore wall are given by

$$\frac{\partial \hat{u}}{\partial \hat{r}}(0, \hat{t}; \hat{z}_i) = 0 \text{ and } \frac{\partial \hat{u}}{\partial \hat{r}}(1, \hat{t}; \hat{z}_i) = 0 \tag{58}$$

For the pore-closure metrics, the nondimensional threshold density is

$$\hat{u}_c = \frac{u_c}{K}. \tag{59}$$

We normalize the threshold-front location $r_c(t; z_i)$ against the empty pore,

$$\hat{r}_c = R^{-1} r_c(t; z_i), \tag{60}$$

such that

$$\hat{r}_c(t; z_i) = \min\{\hat{r} \in [0, 1] : \hat{u}(\hat{r}, \hat{t}; \hat{z}_i) \geq \hat{u}_c\} \tag{61}$$

so $\hat{r}_c(t; z_i)$ decreases from near $\hat{r} = 1$ toward $\hat{r} = 0$ as the populated region advances inward.

Using the length scale R and time scale $1/\lambda_{\max}$, a velocity scale

$$\hat{v} = R\lambda_{\max} \tag{62}$$

is induced. The effective finite-time front velocity conveniently becomes

$$\hat{v}_{\text{eff}}(\hat{t}_1, \hat{t}_2; \hat{z}_i) = \frac{\hat{r}_c(\hat{t}_1; \hat{z}_i) - \hat{r}_c(\hat{t}_2; \hat{z}_i)}{\hat{t}_2 - \hat{t}_1}. \tag{63}$$

The minimum wave speed v^*, dependent on D_u and λ, must incorporate the oxygen-modulated parameter $g(\hat{z}_i)$ such that its dimensionless form becomes

$$\hat{v}^*(\hat{z}_i) = \frac{v^*(z_i)}{R\lambda_{\max}} = \sqrt{\frac{\alpha^2 g(\hat{z}_i)}{2}}. \tag{64}$$

2.7 Analysis of Timescales

The reduced model couples three processes that operate on separated timescales: scaffold-scale cell seeding, scaffold-scale oxygen transport, and pore-scale bridging. The timescale separation justifies the one-way coupling $\hat{\rho}(\hat{z}) \rightarrow \hat{c}(\hat{z}) \rightarrow \hat{u}(\hat{r}, \hat{t}; \hat{z}_i)$, where each field is resolved and passed downstream. It also underlies key assumptions of the oxygen model, including spatial uniformity within a pore and the quasi-steady approximation. We demonstrate that the governing dimensionless groups are merely ratios of these characteristic times.

Oxygen transport occurs on three timescales. $t_{\mathrm{O_2,pore}}$ gives the time for oxygen to equilibrate over the pore by diffusion. Across the scaffold height, a similar diffusive relaxation time is described by t_{diff}. The consumption time t_{cons} is found by linearizing the Michaelis-Menten reaction term at low concentration, $F \approx (V_{\max}\rho_0)/K_m)c$, revealing $(V_{\max}\rho_0)/K_m$ as a first-order rate constant. Therefore,

$$t_{\mathrm{O_2,pore}} = \frac{R^2}{D_c},\ t_{\mathrm{diff}} = \frac{H^2}{D_c},\ t_{\mathrm{cons}} = \frac{K_m}{V_{\max}\rho_0}. \tag{65}$$

The pore-scale cell density possesses two timescales including the time to proliferate, t_{prolif}, and the time to migrate across the pore, t_{mig},

$$t_{\mathrm{prolif}} = \frac{1}{\lambda_{\max}},\ t_{\mathrm{mig}} = \frac{R^2}{D_u}. \tag{66}$$

Both estimates provide lower-bound estimates of their true values; the true proliferation time is modulated by oxygen depletion through $1/(\lambda_{\max} g(\hat{z}_i))$, where $g(\hat{z}_i) \leq 1$, and the degenerate effective diffusivity follows $D_{\mathrm{eff}} = D_u(\hat{u}/K) \leq D_u$.

Set by gravity and adhesion, seeding completes over t_{seed}, after which the timescale for pore-bridging may begin. The timescale for pore bridging, t_{bridge}, is given by the slowest of t_{prolif} and t_{mig}, so $t_{\mathrm{bridge}} \approx \max\{t_{\mathrm{prolif}}, t_{\mathrm{mig}}\}$. Thus, a hierarchy of timescales can be established:

$$t_{\mathrm{O_2,pore}} \ll t_{\mathrm{diff}}, t_{\mathrm{seed}} \ll t_{\mathrm{bridge}}. \tag{67}$$

Because $R \ll H$, the pore-scale and scaffold-scale oxygen diffusion times must follow,

$$\frac{t_{\mathrm{O_2,pore}}}{t_{\mathrm{diff}}} = \left(\frac{R}{H}\right)^2 \ll 1. \tag{68}$$

Oxygen equilibrates across a pore on a significantly shorter timescale than that on which the scaffold-scale oxygen solution $c(z)$ varies axially; all cells in a pore at depth z_i share the common concentration, $c(r, z_i) \approx c(z_i)$, removing any radial dependence of oxygen within a pore and justifying the uniform-pore assumption.

For the quasi-steady oxygen assumption, we see that c can vary over time only through its consumption. If that source were to evolve on the pore bridging scale, the transient

and diffusive terms of (7) would scale as

$$\frac{\partial c}{\partial t} \approx \frac{\Delta c}{t_{\text{bridge}}} \text{ and } D_c \frac{\partial^2 c}{\partial z^2} \approx \frac{\Delta c}{t_{\text{diff}}}, \tag{69}$$

with the ratio

$$\frac{|\partial c/\partial t|}{|D_c \partial^2 c/\partial z^2|} \approx \frac{t_{\text{diff}}}{t_{\text{bridge}}} \ll 1. \tag{70}$$

The transient is negligible, rapidly tracking consumption, and $\partial c/\partial t$ can be dropped. In our model, ρ_{eff} is prescribed and independent of time, so c must be governed by the steady-state equation (8) exactly and requires no initial condition. Given the timescale estimate, the quasi-steady assumption would hold even if the consumption term evolved slowly with time under pore-scale feedback.

The final inequality, $t_{\text{seed}} \ll t_{\text{bridge}}$, merely states that $\hat{\rho}_{\text{eff}}$ is completely established before pore bridging dynamics begin. $t = 0$ is positioned after t_{seed}, rather than at the moment cells are added to the scaffold.

The timescale ratios reappear in the nondimensional parameters. Times for oxygen diffusion and consumption are divided to obtain the Thiele modulus,

$$\phi^2 = \frac{V_{\max} \rho_0 H^2}{K_m D_c} = \frac{H^2/D_c}{K_m/(V_{\max}\rho_0)} = \frac{t_{\text{diff}}}{t_{\text{cons}}}, \tag{71}$$

so $\phi^2 \gg 1$ indicates that cells consume oxygen faster than diffusion can resupply it, producing depletion and attenuating nutrient gradients.

The pore-scale motility-proliferation parameter can similarly be defined as a ratio of the two cell-intrinsic times,

$$\alpha^2 = \frac{D_u}{R^2 \lambda_{\max}} = \frac{1/\lambda_{\max}}{R^2/D_u} = \frac{t_{\text{prolif}}}{t_{\text{mig}}}, \tag{72}$$

so $\alpha^2 \ll 1$ imposes a reaction-dominated regime where cells divide before they spread, consistent with the sharp and slowly advancing Porous-Fisher front, whereas $\alpha^2 \gg 1$ produces a migration-dominated system. Taken together, α^2 gauges how far the tissue front advances per proliferation cycle.

By contrast, the saturation ratios γ_m and γ_s are independent of timescales and merely scale the reaction rates through Monod and Michaelis-Menten kinetics.

ϕ^2 and α^2 emerging as timescale ratios reflects the larger property of reaction-diffusion equations having intrinsic timescales governed by their reaction, which in our multi-scale model include t_{cons} and t_{prolif}. $l \approx \sqrt{D t_{\text{reaction}}}$ gives the intrinsic distance diffusion covers in a single reaction time. A group expressible as the ratio of a diffusion time to reaction time may similarly be read as the ratio of the domain size to this intrinsic length.

2.8 Analysis of Nondimensional Parameters

Nondimensionalization reduces the roughly twenty dimensional inputs of Table 1 into a smaller collection of dimensionless groups organized along $\hat{\rho}(\hat{z}) \to \hat{c}(\hat{z}) \to \hat{u}(\hat{r}, \hat{t}; \hat{z}_i)$. The decisive ϕ^2 and α^2 groups appeared in Section 2.7 as timescale ratios governing the dynamics of diffusion versus reaction. Both also admit equivalent length-scale interpretations, providing the intrinsic distance a substance must travel in one reaction time.

At the pore scale, a cell covers the characteristic distance

$$R_c = \sqrt{\frac{D_u}{\lambda_{\max}}} = \sqrt{D_u t_{\text{prolif}}} \tag{73}$$

in one proliferation time. In other words, R_c gives the distance a cell will migrate before dividing. The motility-proliferation parameter is then given by,

$$\alpha^2 = \left(\frac{R_c}{R}\right)^2, \tag{74}$$

so $\alpha^2 < 1$ indicates that a cell divides before it can bridge the pore, whereas for $\alpha^2 > 1$ migration will span the pore within a division cycle and diffusion dominates. As the effective diffusivity is degenerate and capped by D_u, R_c sets an upper bound on the cell's migration distance.

The Thiele modulus reveals a similar length-scale interpretation. Scaling against the first-order consumption rate $V_{\max}\rho_0/K_m$, oxygen penetrates a characteristic depth

$$L_c = \sqrt{\frac{D_c K_m}{V_{\max}\rho_0}} = \sqrt{D_c t_{\text{cons}}}, \tag{75}$$

before being consumed. Furthermore,

$$\phi^2 = \frac{V_{\max}\rho_0 H^2}{K_m D_c} = \left(\frac{H}{L_c}.\right)^2 \tag{76}$$

When $\phi^2 < 1$, the base remains well-oxygenated; when $\phi^2 > 1$, consumption depletes the supply short of the base, producing gradients that effect heterogeneous pore bridging. Because ϕ^2 is derived from the top-surface density ρ_0, L_c is the shortest and most conservative penetration depth.

The attenuation coefficient $\hat{\beta}$ is the sole determinant of the macroscale cell density $\hat{\rho}(\hat{z})$ across the scaffold's axial depth. When large, cells concentrate near the seeded surface and leave the interior sparse. Because $\hat{\rho}(\hat{z})$ enters both the reaction term of the oxygen equation and the initial amplitude of the pore-scale equation, $\hat{\beta}$ effectively regulates the depth for everything downstream.

The saturation ratios given by γ locate the system on uptake and growth curves. Oxygen consumption given by γ_m drives oxygen availability alongside ϕ^2; for fixed ϕ^2, larger γ_m indicates that the oxygen concentration in medium exceeds the half-saturation level, whereas with smaller γ_m, oxygen uptake will follow the local concentration and steepen the gradient. Similarly, γ_s modulates cell proliferation through the derived group $g(\hat{z}_i)$. Large γ_s can sustain near-maximal proliferation despite oxygen depletion, while small γ_s heightens the sensitivity of cell growth. For the pore-scale equation, depth-dependence enters only through $g(\hat{z}_i)$ as a marker of oxygen availability.

Two velocities describe pore bridging, and both are scaled by $R\lambda_{\max}$. The critical speed is characteristic of the idealized Porous-Fisher wave front $\hat{v}^*(\hat{z}_i)$, but carries no information about domain geometry or initial condition. The speed actually attained by the threshold front is given by $\hat{v}_{\text{eff}}$. $\hat{v}^* \propto \sqrt{\alpha^2 g(\hat{z}_i)}$ illustrates the dependence of v_{eff} on the cell's motility-proliferation ratio and oxygen-modulated proliferation.

2.9 Model Equations

The following nondimensionalized equations are used for simulating the models.

1. Scaffold-scale cell density

$$\hat{\rho}(\hat{z}) = e^{-\hat{\beta}\hat{z}},\ \hat{\rho}(0) = 1$$

2. Scaffold-scale oxygen

$$0 = \frac{\partial^2 \hat{c}}{\partial \hat{z}^2} - \phi^2 \hat{\rho}(\hat{z}) \cdot \frac{\hat{c}}{1 + \gamma_m \hat{c}},$$
$$\phi^2 = \frac{V_{\max} \rho_0 H^2}{K_m D_c} \text{ and } \gamma_m = \frac{c_{\text{media}}}{K_m}.$$
$$\hat{c}(0) = 1,\ \frac{\partial \hat{c}}{\partial \hat{z}}(1) = 0$$

3. Pore-scale cell density

$$\frac{\partial \hat{u}}{\partial \hat{t}} = \alpha^2 \frac{1}{\hat{r}^2} \frac{\partial}{\partial \hat{r}} \left(\hat{r}^2 \hat{u} \frac{\partial \hat{u}}{\partial \hat{r}} \right) + g(\hat{z}_i)\hat{u}(1 - \hat{u}),\ 0 \le \hat{r} \le 1,$$

$$g(\hat{z}_i) = \frac{\gamma_s \hat{c}(\hat{z}_i)}{1 + \gamma_s \hat{c}(\hat{z}_i)}$$
$$\alpha^2 = \frac{D_u}{R^2 \lambda_{\max}} \text{ and } \gamma_s = \frac{c_{\text{media}}}{K_s}.$$
$$\hat{u}(\hat{r}, 0; \hat{z}_i) = \tau(\hat{z}_i) \exp\left(\frac{-(1 - \hat{r})^2}{\hat{\sigma}^2} \right),\ \tau(\hat{z}_i) = \frac{a(z_i)}{K}$$
$$\frac{\partial \hat{u}}{\partial \hat{r}}(0, \hat{t}, \hat{z}_i) = 0,\ \frac{\partial \hat{u}}{\partial \hat{r}}(1, \hat{t}, \hat{z}_i) = 0$$

4. Pore bridging analysis

$$\hat{r}_c(t; z_i) = \min\{\hat{r} \in [0,1] : \hat{u}(\hat{r}, \hat{t}; \hat{z}_i) \geq \hat{u}_c\}$$

$$\hat{v}_{\text{eff}}(\hat{t}_1, \hat{t}_2; \hat{z}_i) = \frac{\hat{r}_c(\hat{t}_1; \hat{z}_i) - \hat{r}_c(\hat{t}_2; \hat{z}_i)}{\hat{t}_2 - \hat{t}_1}.$$

$$\hat{v}^*(\hat{z}_i) = \sqrt{\frac{\alpha^2 g(\hat{z}_i)}{2}}$$

Symbol	**Units**	**Description**
$a(z_i)$	[cells m^{-3}]	Gaussian amplitude; cell density at pore wall
c	[mol m^{-3}]	Dissolved oxygen concentration
c_{media}	[mol m^{-3}]	Oxygen concentration in culture medium
D_c	[m^2 s^{-1}]	Effective oxygen diffusivity in scaffold
D_u	[m^2 day^{-1}]	Cell motility coefficient
H	[m]	Scaffold depth
K	[cells m^{-3}]	Pore-scale cell carrying capacity
K_m	[mol m^{-3}]	Oxygen concentration at half-maximal consumption
K_s	[mol m^{-3}]	Oxygen concentration at half-maximal proliferation
r	[m]	Radial position within a pore
r_c	[m]	Tissue front location
R	[m]	Representative pore radius
t	[day]	Time
u	[cells m^{-3}]	Pore-scale cell density
u_c	[cells m^{-3}]	Threshold cell density within pore
v_{eff}	[m day^{-1}]	Effective finite-time front velocity
$v*$	[m day^{-1}]	Porous-Fisher critical speed
$V_{\max}$	[mol cell^{-1} s^{-1}]	Maximum per-cell oxygen consumption rate
z	[m]	Vertical depth within scaffold
β	[m^{-1}]	Seeding attenuation coefficient
$\lambda_{\max}$	[day^{-1}]	Maximum cell proliferation rate
ρ_0	[cells m^{-3}]	Cell density at scaffold top
ρ_{eff}	[cells m^{-3}]	Prescribed scaffold-scale cell density
σ	[m]	Thickness of adherent cells at pore wall
Ω	[m^3]	Open pore volume

Table 1: Dimensional variables and parameters.

Symbol	Formula	Description
α^2	$\frac{D_u}{\lambda_{max} R^2}$	Motility-proliferation parameter
γ_s	$\frac{c_{\text{media}}}{K_s}$	Oxygen-to-proliferation saturation ratio
γ_m	$\frac{c_{\text{media}}}{K_m}$	Oxygen-to-consumption saturation ratio
ϕ^2	$\frac{V_{max} \rho_0 H^2}{D_c K_m}$	Thiele modulus
$\tau(\hat{z}_i)$	$\frac{a(z_i)}{K}$	Initial amplitude of cell density

Table 2: Nondimensional groups

3 Numerical Simulation Method

3.1 Background on Finite Volume Method

The finite volume method (FVM) solves partial differential equations by discretizing a particular spatial domain, partitioning it into non-overlapping control volumes and monitoring both the average solution value within each volume as well as the flux passing across the faces of neighboring volumes. The spatial discretization is built on the integral, or conservation, form of the governing differential equation rather than its pointwise form. The evolution of each volume is a balance, where the rate of change of some quantity contained within a control volume equals the production within plus the net flux entering through its boundary. This balance allows the FVM to maintain physical conservation across the control volume and the entire spatial domain. Thus, when the governing equation is itself expressed as the divergence of a flux, the FVM technique is the natural choice.

The pore-scale Porous-Fisher model is well suited for FVM for several reasons. First, its diffusion term is provided in conservative form,

$$\alpha^2 \frac{1}{\hat{r}^2} \frac{\partial}{\partial \hat{r}} \left(\hat{r}^2 \hat{u} \frac{\partial \hat{u}}{\partial \hat{r}} \right),$$

i.e., the divergence of migratory flux $\hat{\mathbf{J}}_r$. Therefore, the cell mass conserved by a finite volume discretization occurs exactly through diffusion. A non-conservative finite difference technique could produce mass drift, undermining the pore-closure rates that depend on total cell content. Second, the spherical radial operator contains an apparent singularity at the pore center through the unbounded factor $1/\hat{r}^2$. FVM, however, never evaluates this term at the point; it integrates the flux over a small spherical shell surrounding the center. Because the innermost shell face has both vanishing area and zero flux, due to its boundary condition, the coordinate singularity is conveniently avoided. Third, the diffusion term is degenerate, such that the effective diffusivity $\alpha^2 \hat{u}$ becomes small as the density becomes small, slowing spread in more sparsely populated regions and maintaining a steep front. Capturing the dynamics as a flux balance keeps the front well-behaved and allows discrete fluxes to adapt to the local density. Additionally, the smoothness of the initial condition is advantageous for the flux-based

method. The Gaussian rim is differentiable and strictly positive, so the diffusive flux is well defined at every face from the first time step. In contrast, a discontinuous step rim would have an undefined gradient at its jump and a poorly defined flux at its face, posing difficulties for the finite-volume update.

Mathematically, FVM follows from integrating the governing equation over a control volume and applying the divergence theorem. We define the nonlinear diffusive transport factor,

$$F = \hat{u}\frac{\partial \hat{u}}{\partial \hat{r}}, \tag{77}$$

so the diffusion term may be written as

$$\alpha^2 \frac{1}{\hat{r}^2}\frac{\partial}{\partial \hat{r}}(\hat{r}^2 F), \tag{78}$$

and radial flux as $\hat{\mathbf{J}}_r = -\alpha^2 F$. At the boundaries, the homogeneous Neumann conditions are then equivalent to $F = 0$.

Now consider a representative spherical-shell control volume bounded by inner radius a and outer radius b. Multiplying the governing equation by the spherical volume element $4\pi\hat{r}^2$ and integrating from a to b gives,

$$\frac{d}{d\hat{t}}\int_a^b 4\pi\hat{r}^2\hat{u}d\hat{r} = 4\pi\alpha^2\int_a^b \frac{\partial}{\partial \hat{r}}(\hat{r}F)d\hat{r} + 4\pi\int_a^b \hat{r}^2 g\hat{u}(1-\hat{u})d\hat{r}, \tag{79}$$

where the time derivative reports the change in cell density within a shell. Applying the divergence theorem collapses the diffusion integral into a difference of the flux through the shell's faces,

$$\int_a^b \frac{\partial}{\partial \hat{r}}(\hat{r}F)d\hat{r} = b^2F(b) - a^2F(a), \tag{80}$$

with each term weighted by the surface area of its face, scaling as $\hat{r}^2$.

The volume of the spherical shell is,

$$V = \frac{4\pi}{3}(b^3 - a^3), \tag{81}$$

and the shell-averaged density is defined by

$$U = \frac{1}{V}\int_a^b 4\pi\hat{r}^2\hat{u}\, d\hat{r}. \tag{82}$$

Therefore, UV is the total cell density contained in the shell. The finite-volume update evolves this shell average according to fluxes through the inner and outer faces, together with the local proliferation term. Upon discretizing the flux balance

by indexing the shells, the face fluxes are approximated. Each interior face is shared by two adjacent spherical shells with opposite signs, so summing the balance over all shells leaves only the two boundary fluxes which vanish by the boundary conditions. When these vanish, the total cell mass must be conserved, providing a check for implementation success.

3.2 Simulation Method

The nondimensionalized model is solved along its one-way coupling, with each system solved by a method appropriate to its type. The exponentially decaying scaffold-scale density is available in closed form; the oxygen field is a nonlinear boundary value problem solved by collocation; and the pore-scale cell density evolution employs the finite-volume system described in Section 3.1, advanced in time by a stiff method-of-lines integrator.

The scaffold-scale effective cell density, $\hat{\rho}(\hat{z}) = e^{-\hat{\beta}\hat{z}}$, is evaluated pointwise as needed, both in the oxygen equation and the depth-dependent amplitude of the pore-scale initial condition.

To solve the nonlinear boundary value problem (43) governing the quasi-steady oxygen concentration, the second-order equation $\hat{c}'' = \phi^2 \hat{\rho}(\hat{z}) \cdot \hat{c}/(1 + \gamma_m \hat{c})$ is recast as a first-order system in

$$y_1 = \hat{c},\ y_2 = \hat{c}', \tag{83}$$

with

$$y_1' = y_2,\ y_2' = \phi^2 e^{-\hat{\beta}\hat{z}} \frac{y_1}{1 + \gamma_m y_1} \tag{84}$$

subject to $y_1(0) - 1 = 0$ and $y_2(1) = 0$. A finite-difference collocation solver (bvp4c in MATLAB) is then used to integrate the first-order system. $\hat{c}(\hat{z})$ is specified at each depth, as well as the Monod-style proliferation multiplier $g(\hat{z}_i)$ that enters the pore-scale reaction term. The one-way coupling of the reduced model requires that the oxygen solve is performed only once and is not updated as the pore-scale cell density grows.

At the pore-scale, the radial domain $0 \leq \hat{r} \leq 1$ is partitioned into a mesh of N spherical-shell control volumes with uniform spacing $\Delta\hat{r} = 1/N$. The mesh faces lie at radii given by

$$\hat{r}_{i+1/2} = i\Delta\hat{r} = \frac{i}{N},\ i = 0, 1, ..., N \tag{85}$$

so that a shell i between faces $[\hat{r}_{i-1/2}, \hat{r}_{i+1/2}]$ with center

$$\hat{r}_i = \frac{\hat{r}_{i-1/2} + \hat{r}_{i+1/2}}{2} \tag{86}$$

has the stripped shell volume

$$V_i = \frac{4\pi}{3}(\hat{r}_{i+1/2}^3 - \hat{r}_{i-1/2}^3). \tag{87}$$

The unknown shell-averaged density $U_i(\hat{t})$ in shell i is found by discretizing the shell balance outlined in Section 3.1 and approximating the reaction integral by $V_i g(\hat{z}_i) U_i(1-U_i)$, and then dividing by V_i, allowing the common 4π to cancel and yielding a semi-discrete system where the radial coordinate is discretized while time remains continuous. Thus, the PDE is converted into a coupled system of ordinary differential equations for $U_i(\hat{t})$,

$$\frac{dU_i}{d\hat{t}} = \alpha^2 \frac{\hat{r}_{i+1/2}^2 F_{i+1/2} - \hat{r}_{i-1/2}^2 F_{i-1/2}}{V_i} + g(\hat{z}_i) U_i(1-U_i),\ i = 1, ..., N. \tag{88}$$

For each interior face, $F_{i+1/2}$ approximates the nonlinear diffusive transport factor at the face between shells i and $i+1$. $\hat{u}$ at the face is approximated by the arithmetic mean of the neighboring shell averages, while $\hat{u}_{\hat{r}}$ is approximated by a centered difference:

$$F_{i+1/2} = \frac{U_i + U_{i+1}}{2} \frac{U_{i+1} - U_i}{\Delta \hat{r}},\ i = 1, ..., N-1. \tag{89}$$

The range of indices i is minimized to separately impose conditions at the boundary faces. At the pore center and pore wall, the boundary face transport terms are set to zero, $F_{1/2} = 0$ and $F_{N+1/2} = 0$, enforcing impermeability. It is worth noting however that zero flux will always occur when $\hat{u} = 0$, so $\hat{u}_{\hat{r}} = 0$ may not be enforced. Where $\hat{u} > 0$, as imposed by the Gaussian initial condition, the zero-flux condition becomes equivalent to the homogeneous Neumann condition required particularly at the pore center. Furthermore, at $\hat{r} = 0$ the finite-volume discretization avoids directly evaluating the radial operator. The first control volume begins at the origin, and the area-weighted inner flux $\hat{r}_{1/2} F_{1/2}$ vanishes because $\hat{r}_{1/2} = 0$. This is consistent with the regularity condition $\hat{u}_{\hat{r}}(0, \hat{t}) = 0$ required by a smooth radially symmetric solution.

When the diffusion terms are summed over every shell i, while $F_{1/2} = F_{N+1/2} = 0$, the interior flux terms cancel pairwise because each internal face is shared by two neighboring shells with opposite signs. Therefore, when proliferation is removed, the discrete total mass $\sum_{i=1}^{N} V_i U_i$ is conserved up to time-integration error.

The Gaussian initial condition, providing initial data for the discretized system, is evaluated at shell centers,

$$U_i(0) = \tau(\hat{z}_i) \exp\left(-\frac{(1-\hat{r}_i)^2}{\hat{\sigma}^2}\right),\ \tau(\hat{z}_i) = \min(1, \tau_0 e^{-\hat{\beta}\hat{z}_i}), \tag{90}$$

where the minimum operator protects the amplitude from growing larger than the carrying capacity $\hat{u} = 1$.

Because the spatial discretization is semi-discrete, time is left continuous while the radial coordinate is discretized. Therefore, the pore-scale PDE is converted into a

semi-discrete system of N ordinary differential equations,

$$\frac{d\mathbf{U}}{d\hat{t}} = \mathbf{f}(\mathbf{U}), \tag{91}$$

where $\mathbf{U} = (U_1, ..., U_N)^T$ contains the shell-averaged densities. The i-th component of $\mathbf{f}$ is the finite-volume balance for shell i, consisting of the difference between the diffusive transport at the outer and inner faces together with the local proliferation term, as seen in (88). The method of lines technique is then used to integrate the ordinary differential equations in time. However, the system is stiff because diffusion decays by a rapidly decaying mesh scale. For a mesh of spacing $\Delta\hat{r}$, the fastest diffusive decay scales like $\alpha^2/\Delta\hat{r}^2$, large relative to the timescale of proliferation and front advance. An explicit integrator would require time steps scaling like $\Delta\hat{r}^2\alpha^2$ for stability. As the mesh is further refined, this restriction can become severe. Therefore, the ODE system is advanced using a variable-order, variable-step implicit stiff solver (ode15s in MATLAB), which chooses internal time steps adaptively to contain local error tolerances.

As the pore-scale model is physically meaningful only for densities within $0 \leq \hat{u} \leq 1$, cell averages are checked to ensure they remain within the range over the full simulation. The solver is run with a nonnegativity constraint, holding the lower bound $U_i \geq 0$, and capping at the carrying capacity to maintain the upper bound $U_i \leq 1$. With the strictly positive initial condition, the conservative discretization tends to remain nonnegative; however, this safeguard prevents the system from producing small negative solutions due to the degenerate diffusion and steep front. In well-resolved runs, the cap containing the solution within $[0, 1]$ is not needed and the mass conservation of diffusion is upheld. The check is enforced only as a safeguard to ensure the numerical solution remains physically bounded.

Another numerical sensitivity arises at the pore center, where $\hat{u}(0)$ can rise sharply once the front reaches it. At every output time, $\hat{r}_c$ is calculated by (61); moving outward from the center, the first pair of shells that bracket $\hat{u} = \hat{u}_c$ is identified and $\hat{r}_c$ is found by linear interpolation between them. Only for pore closure visualization is the movement of the threshold front $\hat{r}_c$ mapped onto a Cartesian circle by radial symmetry using $\hat{r} = \sqrt{x^2 + y^2}$, and the finite-volume solution interpolated on points satisfying $\hat{r} \leq 1$, to produce pore cross-sections.

4 Results

Unless otherwise stated, all simulations use the baseline nondimensional parameter set $\hat{\beta} = 5.00$, $\phi^2 = 70$, $\gamma_m = 20$, $\gamma_s = 2.50$, $\alpha^2 = 0.08$, $\tau_0 = 0.60$, $\hat{\sigma} = 0.08$, $\hat{u}_c = 0.50$. To solve the pore-scale model, the finite-volume discretization is performed at mesh resolution $N = 250$.

4.1 Model simulation

Model simulations use the baseline parameter set, so the figures presented differ from one another only in the quantities being varied, namely the seeding condition and scaffold depth. The model proceeds sequentially through three coupled fields: the prescribed scaffold-scale cell density $\hat{\rho}(\hat{z}) \to \hat{c}(\hat{z}) \to \hat{u}(\hat{r}, \hat{t}; \hat{z}_i)$, presenting a narrative that address three primarily questions: whether realistic seeding densities produce meaningful oxygen gradients, how those gradients shape pore-scale bridging, and whether the degenerate Porous-Fisher formulation is necessary to capture the biologically accurate dynamics.

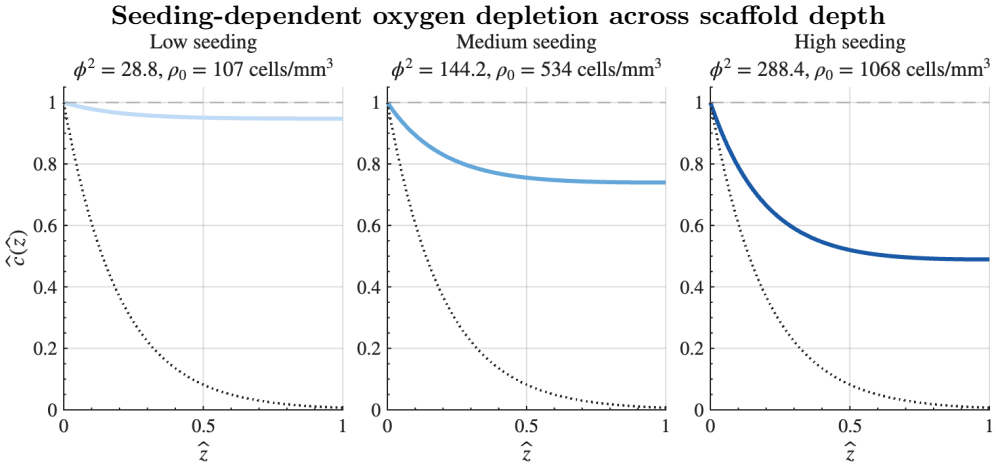

Fig. 2: $\hat{c}(\hat{z})$ (solid) for low, medium, and high seeding conditions (10,000, 50,000, and 100,000 adhered cells per scaffold, respectively). $\hat{\rho}(\hat{z})$ (dotted) is overlaid. $\hat{\beta} = 5.00$ and $\gamma_m = 20$.

Figure 2 establishes that oxygen limitation is a real consequence of seeding rather than a modeling artifact. As the seeding condition increases from low to high, the base oxygen concentration transitions from essentially well-mixed to severely depleted: at low seeding the profile stays near saturation throughout the depth, while at high seeding it falls to near zero at the base. The gradient is steepest near the top surface, mirroring the exponential cell density profile overlaid in the figure — consumption is concentrated where cells are concentrated. The exponential attenuation of $\hat{\rho}(\hat{z})$ therefore partially protects the interior by reducing local consumption, but this protection is overwhelmed once the Thiele modulus grows large. Because all three seeding conditions fall within the biologically plausible range for cryogel scaffolds, the figure confirms that oxygen-limited bridging is an experimentally accessible regime and motivates the rest of the analysis.

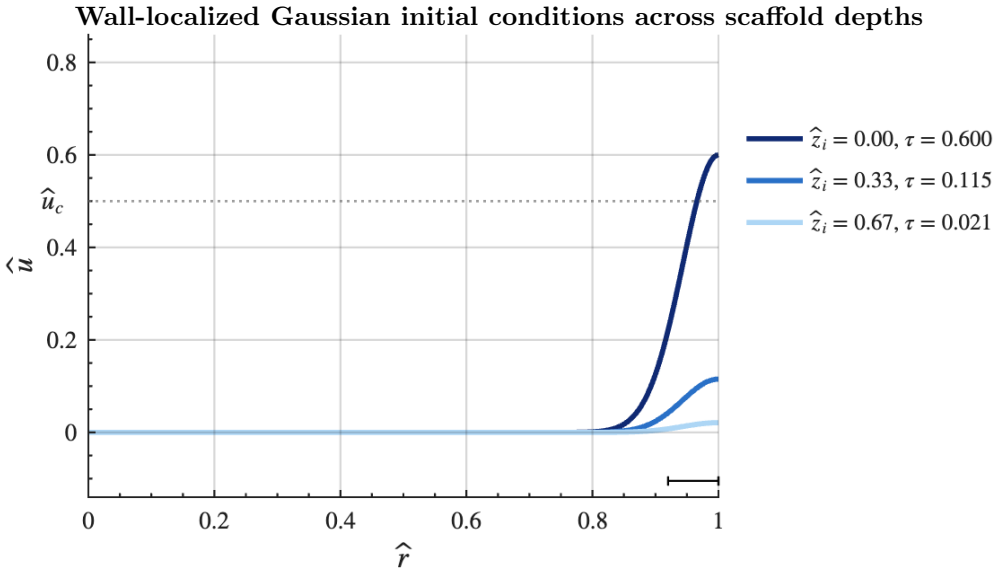

Fig. 3: $\hat{u}(\hat{r}, 0, \hat{z}_c)$ versus $\hat{r}$. Dashed line marks $\hat{u}_c$; the bracket indicates rim width $\hat{\sigma}$. $\tau_0 = 0.60$, $\hat{\sigma} = 0.08$, $\hat{u}_c = 0.50$, and $\hat{\beta} = 5.00$.

The oxygen field couples to the pore scale through two channels: it modulates the proliferation rate via $g(\hat{z}_i)$, and the same exponential attenuation that governs $\rho(\hat{z})$ sets the initial seeding amplitude $\tau(\hat{z}_i)$. Figure 3 shows the resulting initial conditions across depth. The decisive feature is the position of each profile relative to the threshold $\hat{u}_c$: the top-surface pore is seeded above threshold, so it is effectively bridged at $t = 0$, whereas pores deeper in the scaffold begin well below threshold and must rely on migration and proliferation to bridge at all. The narrow rim width confirms the initial mass is tightly wall-localized in every case, supplying the inward density gradient that drives the front. The key point is that depth-dependent heterogeneity is built into the initial condition by $\hat{\beta}$ alone, before oxygen effects are considered; oxygen depletion then compounds it, since deeper pores both start with fewer cells and proliferate more slowly.

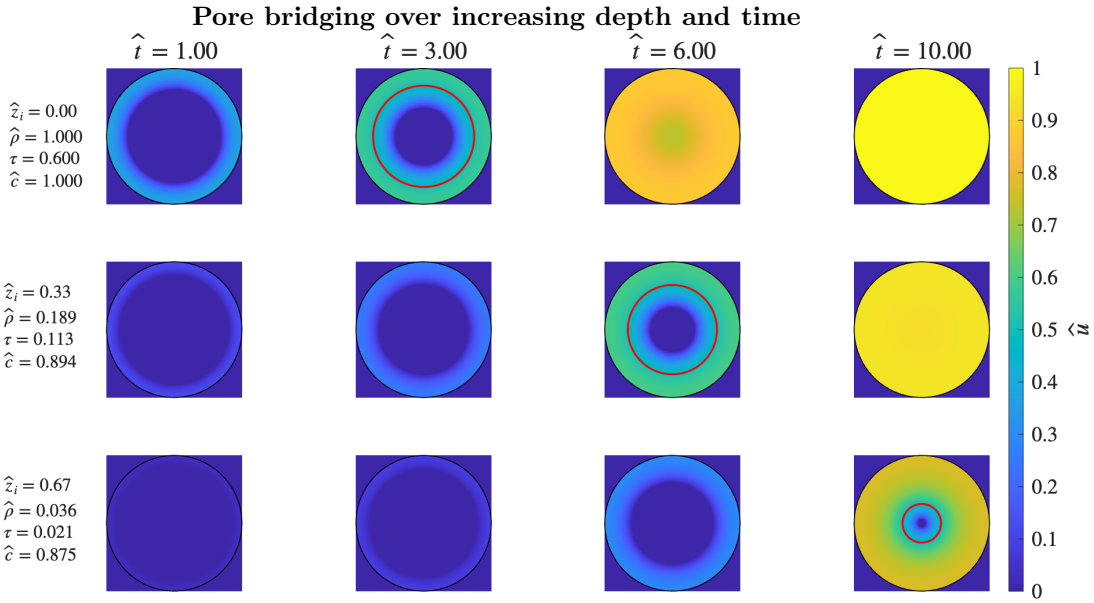

Fig. 4: Pore cross-sections of $\hat{u}(\hat{r}, \hat{r}; \hat{z}_i)$, interpolated onto two-dimensional disks under spherical symmetry. The red contour marks $\hat{u}_c$. The baseline nondimensional parameter set is used.

Figure 4 traces the forward evolution of these initial conditions as pore cross-sections at increasing times and depths. The rows make the compounding effect visually explicit: the top-surface pore fills completely within the simulation window, the mid-depth pore bridges but visibly later, and the deepest pore remains largely unoccupied throughout, with the threshold contour failing to appear at the final time. The progression from complete bridging to outright failure across a single scaffold is the central qualitative prediction of the coupled model.

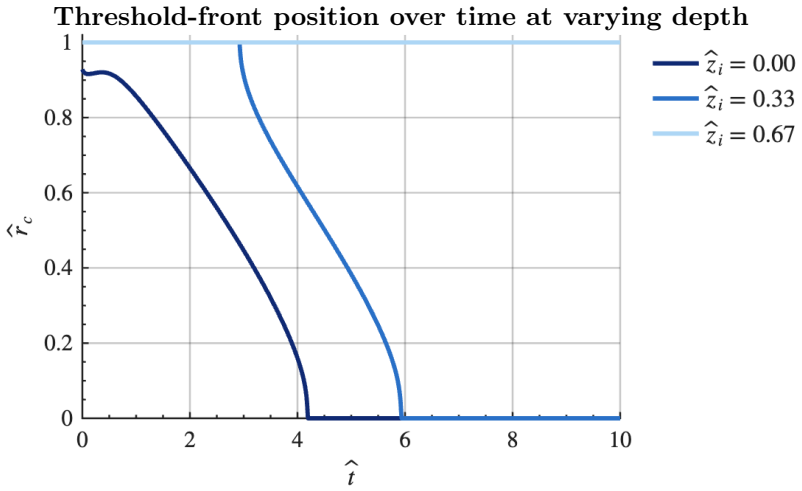

Fig. 5: $\hat{r}_c$ versus $\hat{t}$ at three depths $\hat{z}_i$, shown as raw output without smoothing or enforced monotonicity.

Figure 5 renders this stratification quantitatively as the threshold-front trajectory $\hat{r}_c(\hat{t})$. The surface and mid-depth pores both reach full closure but separated by roughly two dimensionless time units, while the deepest pore shows essentially no inward progress. The contrast establishes that the effect of depth is not a uniform slowing but a qualitative one: beyond a certain depth, the front fails to close within a biologically relevant culture period. The trajectories are shown as raw output without enforced monotonicity, and the minor irregularities reflect the steep front crossing the threshold near the center rather than numerical noise.

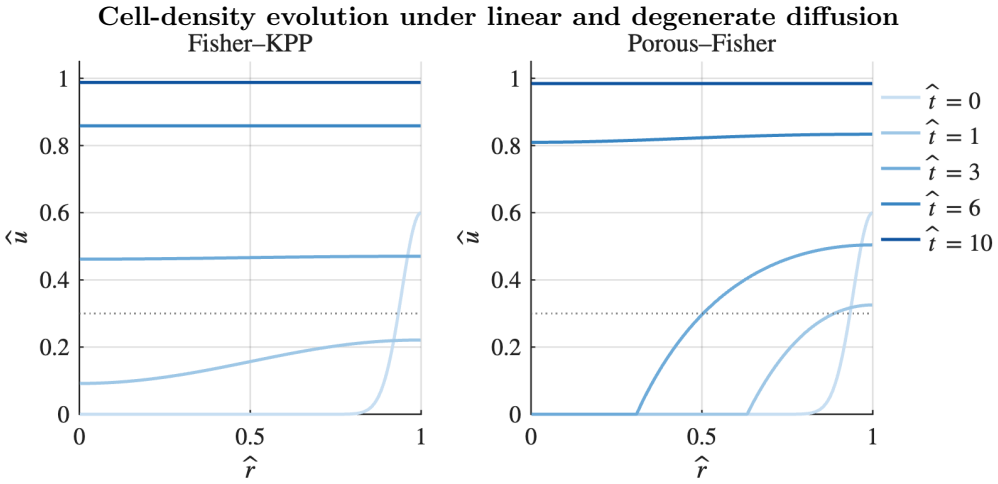

Fig. 6: $\hat{u}$ versus $\hat{r}$ at successive times for the linear Fisher-KPP equation (left) and the degenerate Porous-Fisher equation (right), with identical parameters.

Before summarizing bridging speed across the scaffold, the choice of degenerate diffusion must be justified. Figure 6 compares the density profiles produced by the linear Fisher-KPP and degenerate Porous-Fisher equations under identical parameters. In spherical radial coordinates with oxygen-modulated proliferation, the counterpart Fisher-KPP equation is given by

$$\frac{\partial \hat{u}}{\partial \hat{t}} = \alpha^2 \frac{1}{\hat{r}^2} \frac{\partial}{\partial \hat{r}} \left(\hat{r}^2 \frac{\partial \hat{u}}{\partial \hat{r}} \right) + \frac{\gamma_s \hat{c}(\hat{z}_i)}{1 + \gamma_s \hat{c}(\hat{z}_i)} \hat{u}(1 - \hat{u}), \ 0 \leq \hat{r} \leq 1. \tag{92}$$

Its linear diffusion remains active even at vanishing density, so the initial rim immediately spreads into a broad, smooth wave that populates the pore interior well ahead of any coherent front. Degenerate diffusion vanishes as $\hat{u}$ goes to 0 and instead preserves a sharp, inward-moving edge. Biologically, pore bridging advances as a recognizable tissue boundary, not as a diffuse haze of isolated cells ahead of the population, the behavior the Porous-Fisher model reproduces and the linear model does not.

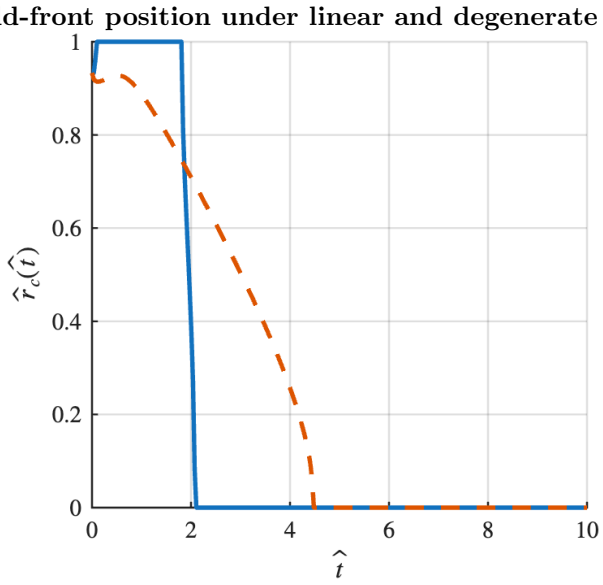

Fig. 7: $\hat{r}_c(\hat{t})$for the linear Fisher-KPP (solid) and Porous-Fisher (dashed) models, with identical parameters.

Figure 7 shows why this distinction matters for the closure measurement itself. Under linear diffusion, $\hat{r}_c(\hat{t})$ abruptly collapses because the broad diffusive tail crosses $\hat{u}_c$ across much of the pore almost simultaneously; the metric reports the arrival of that tail rather than of a front. Under degenerate diffusion, $\hat{r}_c(\hat{t})$ decreases smoothly and progressively. This confirms that the threshold-front velocity $\hat{v}_{\text{eff}}$ is a physically meaningful summary statistic for the Porous-Fisher front but would be misleading for its linear counterpart.

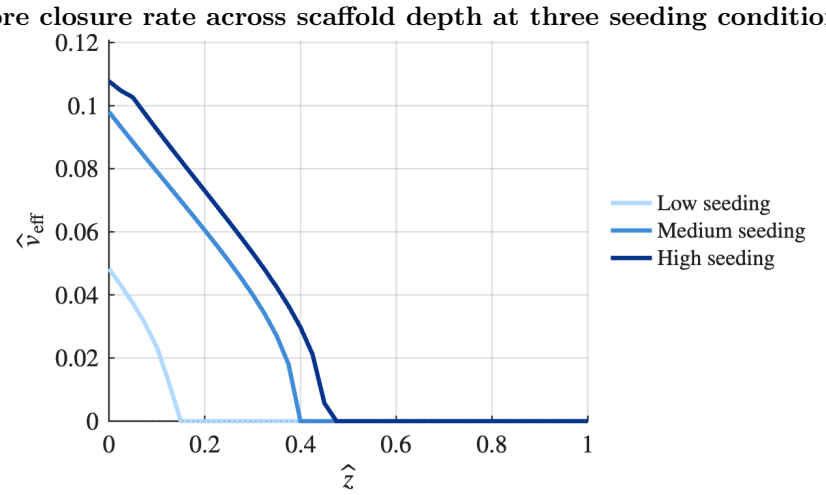

Fig. 8: $\hat{v}_{\text{eff}}$ versus $\hat{z}_i$ for low, medium, and high seeding conditions, corresponding to increasing ϕ^2 and decreasing τ_0. $\hat{v}_{\text{eff}}$ is computed between $\hat{t}_1 = 0.50$ and $\hat{t}_2 = 6.50$.

Figure 8 consolidates the coupled output into the principal result: $\hat{v}_{\text{eff}}$ as a function of depth for each seeding condition. All curves decrease monotonically with depth, but their shapes reveal a regime change. At low seeding, attenuation is gentle and driven almost entirely by the depth dependence of the seeding amplitude, since oxygen remains plentiful. At higher seeding, the near-surface velocity is greater, with more cells proliferating in well-oxygenated conditions, yet the curves fall away far more steeply and reach zero at shallower depths, as oxygen depletion increasingly governs the interior. The result is a non-monotonic trade-off: raising the seeding density accelerates bridging at the surface while contracting the depth over which any bridging occurs. The dependence of this trade-off on the governing parameters ϕ^2 and $\hat{\beta}$ is examined in Section 4.2

4.2 Sensitivity Analysis of Mathematical Model

Whereas Section 4.1 examined the coupled model under the baseline parameter set, this section isolates the influence of the governing dimensionless groups. The analysis is organized by scale: the critical depth and the (ϕ^2, γ_m) map characterize the scaffold-scale oxygen field, while the front-velocity comparisons and the (α^2, g) map characterize the pore-scale bridging response.

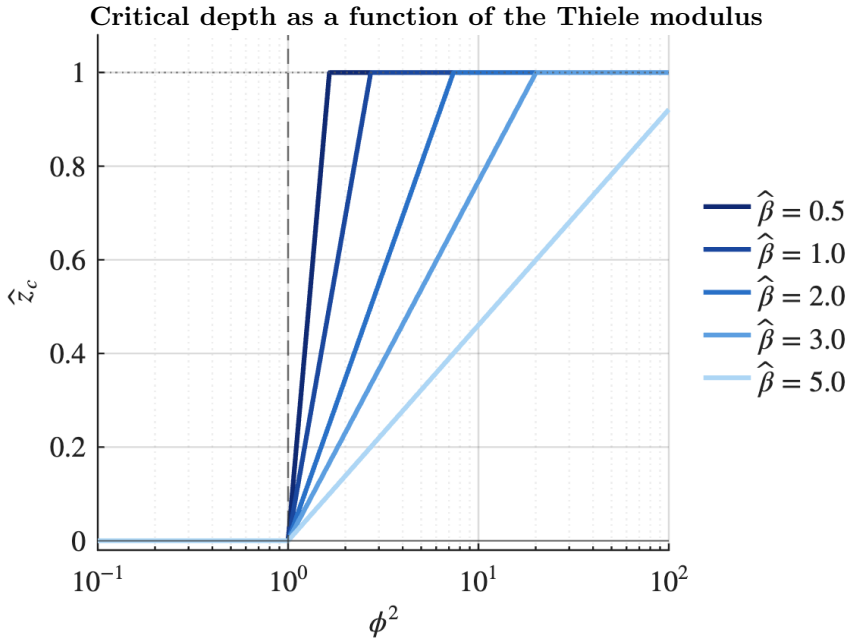

Fig. 9: $\hat{z}_c$ versus ϕ^2 (logarithmic axis) for increasing $\hat{\beta}$.

The onset of oxygen limitation can be located analytically. The local Thiele modulus measures the consumption-to-diffusion ratio at each depth, scaling the global value by the prescribed cell density,

$$\phi^2_{\text{local}} = \phi^2 \hat{\rho}(\hat{z}) = \phi^2 e^{-\hat{\beta}\hat{z}}.$$

Consumption dominates diffusion wherever $\phi^2_{\text{local}} > 1$. Setting $\phi^2_{\text{local}} = 1$ marks the transition, and solving for this critical depth gives

$$\hat{z}_c = \frac{\ln(\phi^2)}{\hat{\beta}}. \tag{93}$$

The closed form makes the spatial onset of oxygen limitation directly predictable from two parameters. Two limits clarify its meaning. When $\phi^2 \leq 1$, the logarithm is non-positive and $\hat{z}_c \leq 0$. In other words, consumption never dominates anywhere, and the scaffold is diffusion-limited throughout. When $\ln(\phi^2) \geq \hat{\beta}$,the critical depth reaches or exceeds the scaffold base, so the entire construct is consumption-dominated.

Figure 9 plots $\hat{z}_c$ against ϕ^2 on a logarithmic axis for several values of $\hat{\beta}$, and both dependencies in the closed form are visible. The logarithmic dependence on ϕ^2 means the consumption-dominated zone deepens only slowly with consumption strength: order-of-magnitude increases in ϕ^2 shift $\hat{z}_c$ by modest increments, and each curve

saturates once it reaches the scaffold base. The dependence on $\hat{\beta}$ runs the opposite way: for fixed ϕ^2, steeper seeding attenuation (larger $\hat{\beta}$ concentrates cells and their consumption near the surface, pushing $\hat{z}_c$ shallower. The figure thus serves as a design map; given experimental estimates of ϕ^2 and β, the consumption-dominated fraction of the scaffold can be read off without solving the oxygen equation.

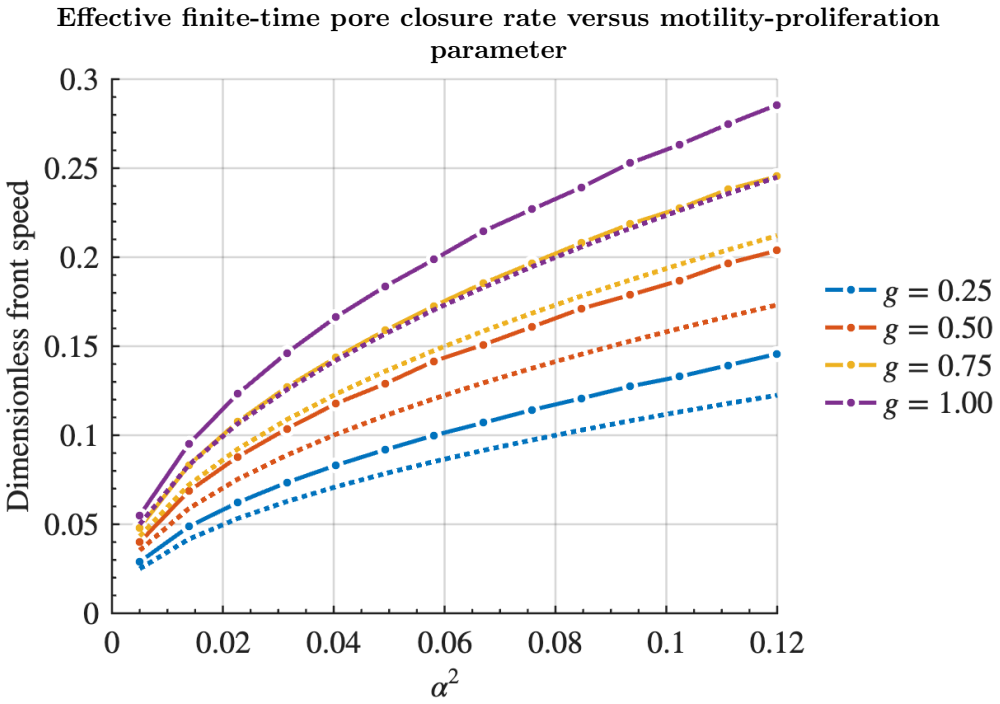

Fig. 10: v_{eff} (dashed line) and $\hat{v}^*$ (dotted line) versus α^2 for fixed proliferation parameter g.

The critical depth describes where oxygen limits proliferation; the next question is how strongly that limitation, encoded in $g(\hat{z}_i)$, sets the front speed, and whether the idealized wave speed predicts the observed one. The minimum traveling-wave speed of the planar Porous-Fisher equation, carried over to the nondimensional pore model, is

$$\hat{v}^* = \sqrt{\frac{\alpha^2 g}{2}},$$

depending on motility and oxygen-modulated proliferation only through their product. Figure 10 plots the operational effective velocity $\hat{v}_{\text{eff}}$ against α^2 alongside $\hat{v}^*$ for several fixed g. Both rise with α^2, but $\hat{v}_{\text{eff}}$ sits above $\hat{v}^*$.

The discrepancy is expected, because $\hat{v}^*$ describes an idealization the pore problem

does not satisfy, and three departures act in the same direction. First, the Gaussian initial condition is strictly positive everywhere and lacks the compact support that the sharp-fronted minimum-speed wave requires; the threshold front therefore advances into a region already carrying a small positive density rather than into true vacuum, raising its apparent speed. Second, the spherical operator carries the curvature term $2/r$, which has no analog in the planar derivation of $\hat{v}^*$; as the front converges inward and r decreases, this term grows and concentrates the inward flux through shrinking shells, accelerating the front beyond the constant planar speed. Third, the pore is a finite domain, so the front reaches the center before relaxing onto its asymptotic speed. Consequently $\hat{v}^*$ is best read as a lower reference rather than a prediction. The gap between $\hat{v}_{\text{eff}}$ and $\hat{v}^*$ quantifies the combined contribution of initial condition, geometry, and finite-domain effects, which are largest in the slow, reaction-dominated regime and recede as motility increases.

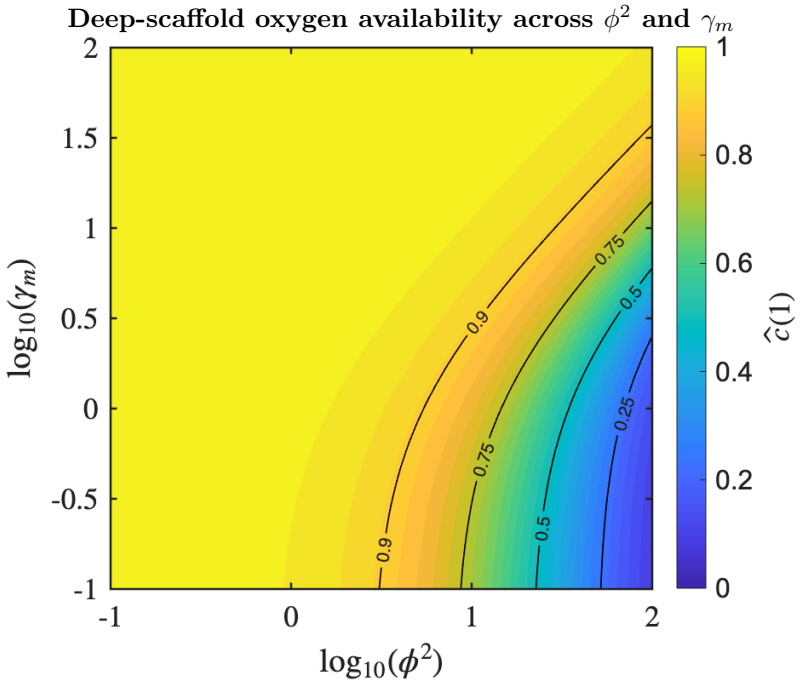

Fig. 11: Oxygen concentration at the base $\hat{c}(\hat{z} = 1)$ over the (ϕ^2, γ_m) plane (logarithmic axes). Contour lines at select oxygen levels.

The remaining figures sweep the parameter pairs that govern each scale jointly. The quasi-steady oxygen field is controlled, for fixed $\hat{\beta}$, by exactly two nondimensional groups: ϕ^2 and γ_m. These serve as the natural axes for a map of deep-scaffold

oxygenation. The two play complementary roles in the consumption term

$$\phi^2 \hat{\rho}(\hat{z}) \frac{\hat{c}}{1 + \gamma_m \hat{c}},$$

where ϕ^2 sets the overall magnitude of consumption relative to diffusion, while γ_m locates the kinetics on the Michaelis–Menten curve. Figure 11 maps the base concentration $\hat{c}(\hat{z} = 1)$ over this plane.

The map separates into two limiting behaviors that explain why the pairing is informative. At large γ_m, uptake saturates and approaches a zeroth-order rate $V_{\max}\hat{\rho}$ independent of $\hat{c}$; consumption proceeds at full rate even as oxygen falls, so increasing ϕ^2 drives strong depletion and the base empties readily. At small γ_m, uptake is first-order in $\hat{c}$ and therefore self-limiting; as oxygen falls, so does consumption, which protects the base and demands a much larger ϕ^2 before appreciable depletion occurs. The baseline of $\gamma_m = 20$ lies in the saturated regime, confirming that under standard conditions consumption near the surface is effectively concentration-independent and depletion at depth is governed primarily by ϕ^2. The figure complements the single-parameter critical-depth analysis by showing how kinetic regime, not just consumption strength, conditions oxygen availability.

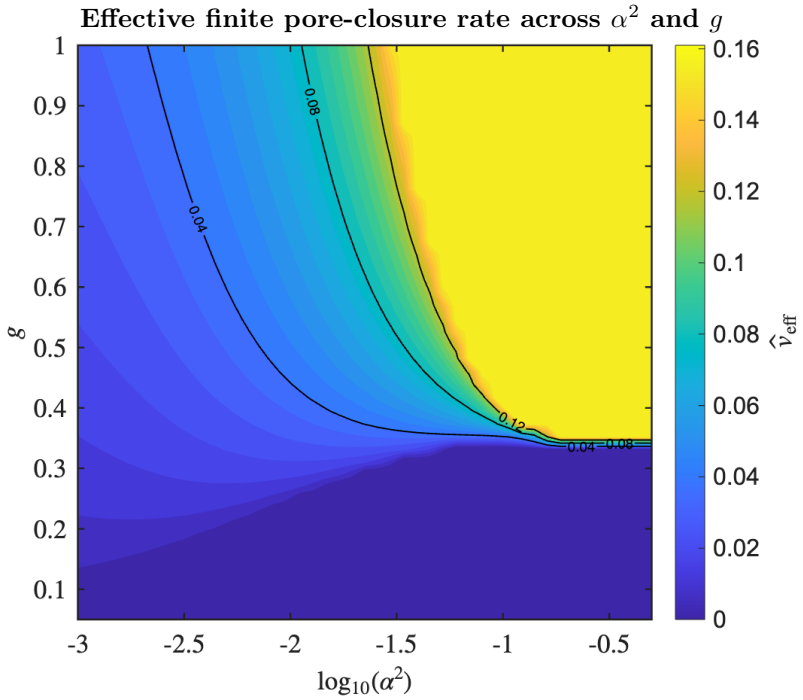

Fig. 12: $\hat{v}_{\text{eff}}$ over the (α^2, g) plane, with α^2 on a logarithmic axis and contour lines at select velocity levels. $\hat{v}_{\text{eff}}$ computed between $\hat{t}_1 = 1.00$ and $\hat{t}_2 = 7.00$

The analogous pairing for the pore scale is (α^2, g), the two groups remaining in the nondimensional Porous-Fisher equation once depth dependence is absorbed into $g(\hat{z}_i)$. Together they determine front speed: α^2 is the motility-to-proliferation ratio and g the oxygen-modulated proliferation rate. Figure 12 maps $\hat{v}_{\text{eff}}$ over this plane with α^2 on a logarithmic axis.

Because $\hat{v}^* \propto \sqrt{\alpha^2 g}$, contours of constant speed track curves of approximately constant $\alpha^2 g$, and the map indeed shows velocity rising toward the upper-right where both parameters are large and falling toward the lower-left where either is small. The product structure means motility and proliferation are partially interchangeable — weak proliferation can be offset by stronger migration, and vice versa — so no single parameter alone determines whether a pore bridges. The map also exposes a feature absent from the idealized speed: a low-g floor, below which $\hat{v}_{\text{eff}}$ remains negligible across the full range of α^2. In this regime proliferation is too weak to lift density above the threshold within the measurement window, so no coherent front forms regardless of motility. This floor marks the practical boundary of oxygen-limited bridging failure and connects directly to the depth-stratified behavior of Section 4.1: as g falls with depth, a pore that crosses below this floor ceases to bridge altogether.

4.3 Convergence of Numerical Method

The finite-volume scheme was adopted because the pore-scale equation is naturally expressed as the divergence of a flux, and a conservative discretization should therefore preserve total cell mass exactly under diffusion alone. The two tests below verify the method against this design property and against its own spatial resolution: the first confirms that the discretization and boundary conditions conserve mass, and the second confirms that the reported quantity of interest, $\hat{v}_{\text{eff}}$, is resolution-independent at the working mesh.

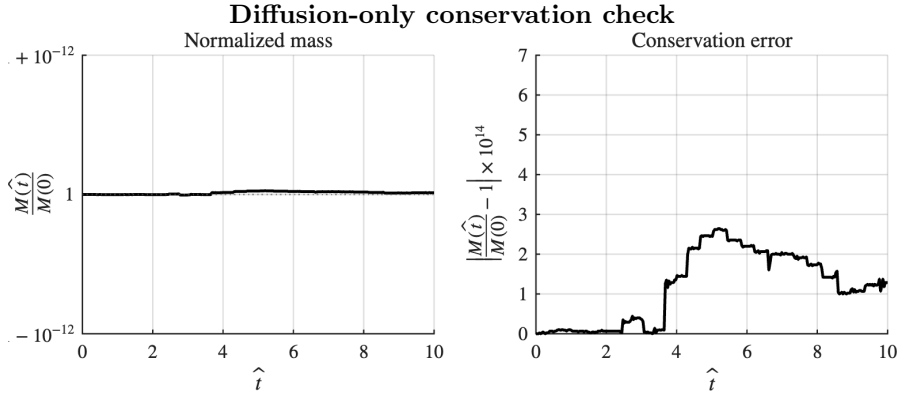

Fig. 13: ($g = 0$) to suppress proliferation and isolate diffusion under no-flux conditions. Error remains on the order of 10^{-14}.

The first test isolates diffusion by suppressing proliferation ($g = 0$), so that the no-flux boundary conditions should leave the total mass

$$\int_0^1 4\pi\hat{r}^2 d\hat{r}$$

unchanged for all time. This is the cleanest available check, because any drift in mass would have to originate in the flux discretization rather than in the reaction term. Figure 13 tracks the normalized mass $M(\hat{t})/M(0)$ and its absolute error, $|M(\hat{t})/M(0) - 1|$. The normalized mass remains indistinguishable from unity throughout the simulation, and the error stays on the order of 10^{-14}, demonstrating that approximately no mass is created or lost. This is the expected consequence of the shell construction: interior face fluxes are shared between adjacent shells with opposite sign and cancel pairwise when summed, leaving only the two boundary fluxes, which the no-flux conditions set to zero. The test validates the spatial discretization and its boundary treatment independently of the time integrator and the reaction kinetics.

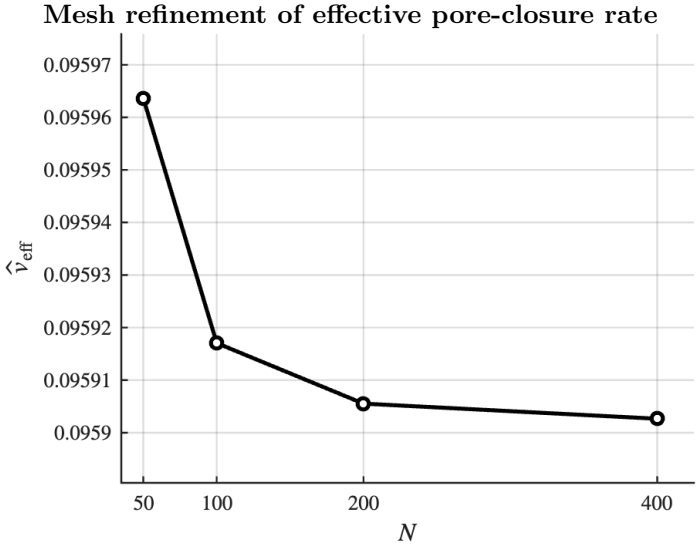

Fig. 14: $\hat{v}_{\text{eff}}$ at mesh resolutions $N = 50, 100, 200, 400$, demonstrating convergence under refinement and justifying the working resolution.

Conservation guarantees the scheme is faithful but not that it is adequately resolved; the steep, degenerate Porous-Fisher front is the feature most sensitive to mesh spacing, and an under-resolved front introduces numerical diffusion that inflates the apparent propagation speed. Figure 14 therefore reports $\hat{v}_{\text{eff}}$ at successively refined meshes, $N = 50, 100, 200, 400$. The velocity decreases monotonically with refinement and the increments shrink rapidly: the change between the two finest meshes is on the order of 10^{-15}, , while the coarsest mesh visibly overestimates the speed, consistent with

excess numerical spreading of the front. The convergence confirms that the working resolution $N = 250$ lies within the estimate where further refinement has negligible effect on the reported velocities, justifying its use across the simulations of Sections 4.1 and 4.2.

5 Conclusion and Discussion

This thesis aimed to investigate causes of heterogeneous tissue growth in cryogel scaffolds by linking scaffold-scale cell density distributions, oxygen depletion, and individual pore bridging. The one-way coupling $\hat{\rho}(\hat{z}) \to \hat{c}(\hat{z}) \to \hat{u}(\hat{r}, \hat{t}; \hat{z}_i)$ was used to isolate these specific mechanisms. This reduced system relied on the separation of timescales, $t_{\mathrm{O}_2,\mathrm{pore}} \ll t_{\mathrm{diff}}, t_{\mathrm{seed}} \ll t_{\mathrm{bridge}}$, which further justified a number of mathematical assumptions declared at the start.

A central finding was that depth-dependent heterogeneity in pore bridging arises from two mechanisms, which act in the same direction. The seeding attenuation $\hat{\beta}$ governs the exponentially decaying cell density over the scaffold's depth and feeds directly into the pore-scale initial amplitude $\tau(\hat{z}_i)$. Oxygen depletion compounds this effect by reducing the Monod-style proliferation multiplier $g(\hat{z}_i)$; deeper pores starting with fewer cells due to cell density attenuation are also most vulnerable to oxygen-depleted zones. The ultimate consequence of these effects are monitored by the effective finite-time pore closure rate.

Nondimensionalization scheme and numerical simulations sharpened this picture significantly. The depth-dependent local Thiele modulus yields a closed-form critical depth, $\hat{z}_c = \ln(\phi^2)/\hat{\beta}$, that predicts the transition between consumption-dominated regions and diffusion-dominated regions. (ϕ^2, γ_m) and (α^2, g) parameter sweeps locate regimes of severe depletion and bridging failure. Comparison of the measured front velocity with the idealized planar wave speed $\hat{v}^*$ shows that the latter is best interpreted as a lower reference, as the pore's spherical curvature, finite-pore domain, and Gaussian initial condition all elevate the tissue-front speed above $\hat{v}^*$.

The model's reductions are also its primary limitations. By freezing the oxygen field, additional consumption by pore-scale proliferation is not accounted for; the model is likely to underestimate oxygen depletion, particularly at later culture times and densely-bridged regions. Similarly, the scaffold-scale cell density is prescribed, rather than evolved, excluding any dynamic cell redistribution. In particular, interconnectivity of the macroporous network is not accounted for by the idealized spherical pore domains.

Despite these reductions, the framework can be parameterized beyond cryogels and applied to various macroporous scaffolds. In making the onset and spatial extent of oxygen limitation predictable from a small set of nondimensionalized groups, the model offers a method for selecting scaffold geometries and culture conditions to favor homogeneous cell growth allowing for well integrated tissue.

References

[1] Hixon, K.R., Lu, T., Sell, S.A.: A comprehensive review of cryogels and their roles in tissue engineering applications. Acta Biomaterialia **62**, 29–41 (2017)

[2] Cagle, A.L., Szulc, E.L., Flaggert, J., Arias, Y., Nikhar, A., Tadio, D., Durant, A., Gitajn, I.L., Hixon, K.R.: Keratin additive for cellular adhesion in transcutaneous prosthetics. Journal of Tissue Engineering and Regenerative Medicine **17** (2025)

[3] Cheng, G., Markenscoff, P., Zygourakis, K.: A 3d hybrid model for tissue growth: The interplay between cell population and mass transport dynamics. Biophysical Journal **97**, 401–414 (2009)

[4] Mokhtari-Jafari, F., Amoabediny, G., Haghighipour, N., Zarghami, R., Saatchi, A., Akbari, J., Salehi-Nik, N.: Mathematical modeling of cell growth in a 3d scaffold and validation of static and dynamic cultures. Engineering in Life Sciences **16**, 290–298 (2016)

[5] Buenzli, P.R., Lanaro, M., Wong, C.S., McLaughlin, M.P., Allenby, M.C., Woodruff, M.A., Simpson, M.J.: Cell proliferation and migration explain pore bridging dynamics in 3d printed scaffolds of different pore size. Acta Biomaterialia **114**, 285–295 (2020)

[6] Edwards, S.L., Church, J.S., Alexander, D.L.J., Russell, S.J., Ingham, E., Ramshaw, J.A.M., Werkmeister, J.A.: Modeling tissue growth within nonwoven scaffold pores. Tissue Engineering Part C: Methods **17** (2011)

[7] Browning, A.P., Maclaren, O.J., Buenzli, P.R., Lanaro, M., Allenby, M.C., Woodruff, M.A., Simpson, M.J.: Model-based data analysis of tissue growth in thin 3d printed scaffolds. Journal of Theoretical Biology **528**, 110852 (2021)

[8] Magliaro, C., Mattei, G., Iacoangeli, F., Cori, A., Piemonte, V., Ahluwalia, A.: Oxygen consumption characteristics in 3d constructs depend on cell density. Frontiers in Bioengineering and Biotechnology **7**, 251 (2019)

[9] Simpson, M.J., McCue, S.W.: Fisher–kpp-type models of biological invasion: open source computational tools, key concepts and analysis. Proceedings of the Royal Society A (2024)

[10] Satnoianu, R.A., Maini, P.K., Garduño, F.S., Armitage, J.P.: Travelling waves in a nonlinear degenerate diffusion model for bacterial pattern formation. Discrete and Continuous Dynamical Systems **1** (2001)

[11] Fadai, N., Simpson, M.J.: New travelling wave solutions of the porous–fisher model with a moving boundary. Journal of Physics A: Mathematical and Theoretical **53** (2020)

[12] Del Castillo, L.F., Silva, A.R., Hernández, S.I., Aguilella, M., Andrio, A., Mollá, S., Compan, V.: Diffusion and monod kinetics model to determine in vivo human corneal oxygen-consumption rate during soft contact lens wear. Journal of Optometry **8** (2015)